CHALMERS
UNIVERSITY OF TECHNOLOGY

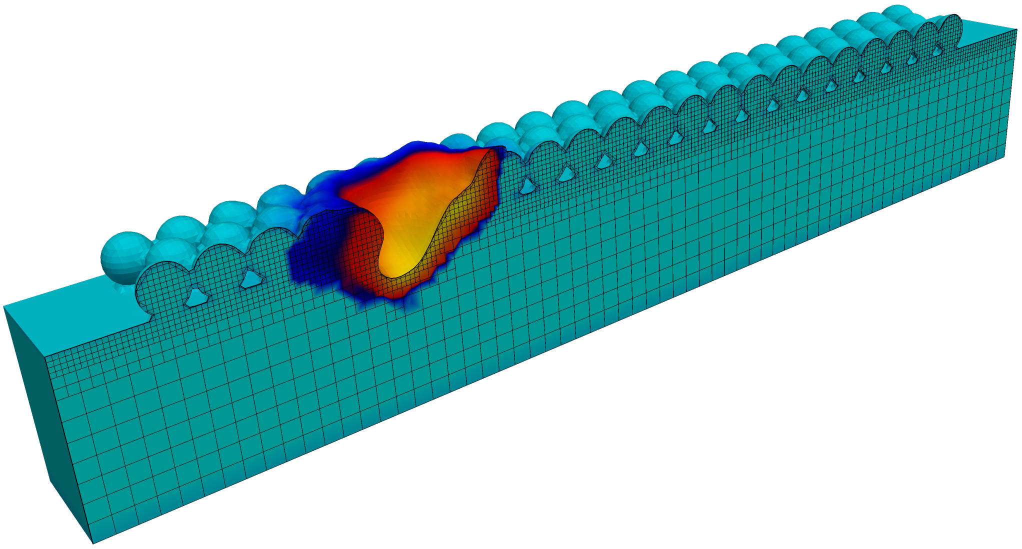

Modeling of Temperature Dependent Surface Tension Forces

Validation of a Temperature Dependent Surface Tension Framework with Application to Powder Bed Melt Pool Dynamics

Master's thesis in Applied Mechanics

Victor Nilsson

Department of Mechanics and Maritime Sciences
CHALMERS UNIVERSITY OF TECHNOLOGY
Gothenburg, Sweden 2019

Master's thesis 2019:01

Modeling of Temperature Dependent Surface Tension Forces

Validation of a Temperature Dependent Surface Tension Framework with Application to Powder Bed Melt Pool Dynamics

Victor Nilsson

Department of Mechanics and Maritime Sciences
Division of Fluid Mechanics
Name of research group (if applicable)
Chalmers University of Technology
Gothenburg, Sweden 2019

Modeling of Temperature Dependent Surface Tension Forces
Validation of a Temperature Dependent Surface Tension Framework
with Application to Powder Bed Melt Pool Dynamics
Victor Nilsson

© Victor Nilsson, 2019.

Supervisor: Johan Göhl, Andreas Mark, Fraunhofer Chalmers Centre
Examiner: Srdjan Sasic, Department of Mechanics and Maritime Sciences

Master's Thesis 2019:01
Department of Mechanics and Maritime Sciences
Division of Fluid Mechanics
Chalmers University of Technology
SE-412 96 Gothenburg
Telephone +46 31 772 1000

Cover: .

Typeset in LaTeX
Printed by [Name of printing company]
Gothenburg, Sweden 2019

Modeling of Temperature Dependent Surface Tension Forces
Validation of a Temperature Dependent Surface Tension Framework with Application to Powder Bed Melt Pool Dynamics
Victor Nilsson
Department of Mechanics and Maritime Sciences
Chalmers University of Technology

Abstract

One of the challenges with CFD simulations of metal AM is to properly model the temperature dependent surface tension force driving the melt pool flow. High density ratio multiphase flows, as between the gas and the liquid metal in melt pool flow, are considered difficult to model due to the generation of spurious currents at the interface. At Fraunhofer Chalmers Center (FCC) a state-of-the-art CFD solver, IBOFlow is developed. In this project the existing surface tension framework in IBOFlow is improved and extended. A temperature dependent surface tension model together with a thermo-capillary force is proposed. The new surface tension framework is assessed and validated so that the melt pool dynamics of metal AM is accurately modeled.

Different curvature estimation techniques and a technique for calculating the interface normal direction are thoroughly tested and evaluated in order to reduce the influence of spurious currents on the results. The numerically calculated curvature and pressure is evaluated and validated against analytical results for a case involving a static droplet in equilibrium. Further more a temperature dependent surface tension model is also proposed and validated together with a thermo-capillary surface tension force. The benchmark case to evaluate the temperature dependent surface tension and the thermo-capillary surface tension force include a comparison with thermo-capillary cavity flow.

The result of the static droplet case show a substantial improvement when calculating the interface curvature and pressure difference across the interface, with results in line with exact analytical calculations. Furthermore, these improvements also substantially reduce the spurious currents around the interface. The temperature dependent surface tension model and the thermo-capillary surface tension force are validated against an analytical solution and compared to other numerical results of the thermo-capillary cavity flow. The results show perfect agreement with analytical values and outperform other numerical studies on the subject. The improved and extended surface tension framework is then used to demonstrate simulate a single line melt of a selective laser melting process on a powder bed.

Keywords: Surface Tension, IBOFlow, computational fluid dynamics, CFD, volume of fluid, VOF, selective laser melting, SLM, multiphase flow.

Acknowledgements

This thesis work was carried out at Fraunhofer-Chalmers Research Centre for Industrial Mathematics. Firstly I would like to thank my supervisor Johan Göhl for his support and enthusiasm throughout this project. Many thoughtful discussion has been carried out with Johan and he has taught me a great deal leading to the finalization of this project. I would also like to thank my supervisor Andreas Mark. His guidance and motivation has pushed the project through critical points. Lastly, I am grateful to all the personal at FCC for the warm welcome I have received and the interest that has been shown in my thesis.
This research has been partly carried out in a Centre for Additive Manufacturing – Metal (CAM2) in a joint project financed by Swedish Governmental Agency of Innovation Systems (Vinnova), coordinated by Chalmers University of Technology.

Victor Nilsson, Gothenburg, January 2019

Contents

List of Figures **xi**

List of Tables **xiii**

1 Introduction **1**
1.1 Background 1
1.2 Aim 3

2 Additive Manufacturing **5**
2.1 Selective Laser Melting 5
2.1.1 Selective Laser Melting System 5
2.1.2 Process cycle and Process parameters 6
2.1.3 AM materials 7
2.2 Physical phenomena of SLM 7

3 Surface Tension force balance **9**
3.1 Dimensionless groups in metal AM 9
3.2 Surface tension 10
3.2.1 Derivation of surface force balance 10
3.2.2 Normal force balance 13
3.2.3 Tangential force balance 13

4 Modeling framework **15**
4.1 Governing equations 15
4.1.1 Conservation of Mass 15
4.1.2 Conservation of Momentum 16
4.1.3 Conservation of Energy 17
4.1.4 Volume of Fluid 17
4.2 Numerical solution procedure 18
4.3 Volume fraction advection model 19
4.4 AM framework 19
4.4.1 Laser model 19
4.4.2 Material models 20
4.4.3 Phase change model 20
4.4.4 Surface tension model 20
4.4.5 AM Modeling limitations 22

5 Improvements to the Surface Tension Framework 23
5.1 Interfacial Smoothing 23
5.2 Height functions 24
5.2.1 Curvature calculation in 2D 26
5.2.2 Curvature calculation in 3D 26
5.3 Temperature dependent surface tension 27
5.4 Tangential surface force 27

6 Simulations 29
6.1 Static droplet in equilibrium 29
6.1.1 2D curvature evaluation 31
6.1.2 3D curvature evaluation 32
6.2 Tangential surface tension force validation 34
6.2.1 Spatial and Temporal convergence 35
6.3 Single line melt simulation 36
6.3.1 Simulation setup and process parameters 37
6.3.2 Material properties 38

7 Results 41
7.1 Curvature Evaluation 41
7.1.1 Static Drop in 2D 41
7.1.2 Static Drop in 3D 45
7.2 Thermo-capillary cavity flow 51
7.3 Single line melt 54

8 Conclusion 57

Bibliography 59

List of Figures

2.1 Depiction of a typical Selective Laser Melting machine 6
2.2 Physical phenomena as a laser melts a metal particle bed. 8

3.1 Fluid-fluid interface, ρ, μ belonging to upper surface (+) and $\hat{\rho}, \hat{\mu}$ belonging to lower surface (-). 11
3.2 Control volume around the surface interface, where ε denote the length elements 11

5.1 Inwards normal of the interface of a circle. 24
5.2 Height function summation at VOF interface (2D) 25

6.1 Static droplet in equilibrium. 30
6.2 Thermo-capillary cavity flow setup with temperature boundary condition, grey indicate phase 1 and green phase 2. 34
6.3 Mesh convergence study, mesh sizes. 36
6.4 Particle bed bead arrangement 37
6.5 Mesh refinement at VOF edge 38

7.1 Error norms of the curvature error κ_{error}, L_1, (left) and , L_∞, (right). 42
7.2 Pressure, numerical and exact across droplet $\frac{\rho_2}{\rho_1} = 1$ 43
7.3 Pressure, numerical and exact across droplet $\frac{\rho_2}{\rho_1} = 10^2$ 44
7.4 Pressure, numerical and exact across droplet $\frac{\rho_2}{\rho_1} = 10^4$ 44
7.5 L_1 norm of κ (left) and L_∞ norm of κ (right) for different curvature estimations calculations. 45
7.6 Curvature error, κ_{error}, using different curvature calculation techniques 46
7.7 Velocity around VOF edge, curvature calculated using, $\nabla\alpha$, (left), $\nabla\tilde{\alpha}$ (middle), and using Height functions for $\rho_2/\rho_1 = 1$. 47
7.8 Velocity around VOF edge, curvature calculated using, $\nabla\alpha$, (left), $\nabla\tilde{\alpha}$ (middle), and using Height functions for $\rho_2/\rho_1 = 10^2$. 47
7.9 Velocity around VOF edge, curvature calculated using, $\nabla\alpha$, (left), $\nabla\tilde{\alpha}$ (middle), and using Height functions for $\rho_2/\rho_1 = 10^4$. 47
7.10 Pressure, numerical calculations and exact across drop $\frac{\rho_2}{\rho_1} = 10^0$ . . . 49
7.11 Pressure, numerical calculations and exact across drop $\frac{\rho_2}{\rho_1} = 10^2$ . . . 49
7.12 Pressure, numerical calculations and exact across drop $\frac{\rho_2}{\rho_1} = 10^4$ . . . 50
7.13 Temporal convergence study 51
7.14 Mesh convergence study 52
7.15 Single line melt with no surface tension 54

7.16 Single line melt with constant surface tension 55
7.17 Single line melt with temperature dependent surface tension 56

List of Tables

6.1 VOF interface curvature estimation 2D 32
6.2 VOF interface curvature estimation 33
6.3 Material properties of Ti-6Al-4V 39
6.4 Material properties of Argon 39

7.1 2D: Error norms for different curvature calculation methods for increasing density ratios 42
7.2 3D: Error norms for different curvature calculation methods for increasing density ratios 48
7.3 Mesh study thermo-capillary cavity 53
7.4 Height at cavity ends comparison 53

1

Introduction

In this chapter a background of the metal additive manufacturing technique is presented together with the aim of this thesis.

1.1 Background

Additive manufacturing (AM) is believed to be next generation technology. With a more than 20 year old history it has now become competitive with traditional manufacturing techniques in terms of cost, speed, reliability and accuracy [1]. Some research claim that static and fatigue properties of 3D printed steel grades, aluminum alloys and titanium alloys typically meet or even exceed properties of cast or wrought counterparts [2]. Additive manufacturing has been enabled due to developments in manufacturing and computing techniques such as Computerized Numerical Control (CNC), Computer Aided Design (CAD) and high-power lasers. The working principle of additive manufacturing is layer-by-layer build up. Initially a 3D digital design of a component is drawn using a CAD software. The digital component is tessellated into triangles which in turn is mathematically cross-sectioned into small 2D layers. The physical build up is made by adding and joining thin fabricated layers on top of each other until a three-dimensional component is made. The direct link between digital design and physical component, without the need to employ traditional manufacturing processes such as drilling, bending, and cutting makes AM a rapid prototyping and manufacturing technique [3, 4, 5].

In metal AM the intrinsic dynamics of the melt pool is of great concern. High temperature cause the metal to melt and liquefy. The dynamics of the liquid metal is governed by the Navier-Stokes equations. The low Bond number (Bo) and the high Laplace number (La) for liquid metals, such as titanium alloys, indicate that surface tension forces dominate and gravitational and viscous forces are small [6]. Problems arise when modeling the surface tension force. Due to a discretization imbalance between the curvature and the associated pressure gradient artificial velocities appear at the interface. These velocities grow in magnitude and can deform the interface. The curvature in the current surface tension model has been revised using height functions and an improved interface normal calculation method. Furthermore the temperature dependent surface tension material property of liquid metals in conjunction with sharp temperature gradients lead to strong thermal-capillary forces in the melt pool.

There are different techniques for modeling the melt pool and the heat transfer during metal AM. Some of the techniques used include finite element method (FEM) [7], Lattice Boltzmann methods (LBM) [5], geometry-based simulations [8] and computational fluid dynamics (CFD) [4]. In the literature several numerical simulations of a single line melt on a powder bed can be found. A review of FEM simulations are located in [9]. These FEM based simulations are generally used for simulating the heat distribution in the building material and the substrate and calculate residual stress. These simulations generally do not model the fluid flow of the individual melting particles. Instead they treat the powder as a homogeneous continuum with effective thermo-mechanical properties. This formulation miss out the small scale physics involved in AM such as local consolidation of particles. In [5] a 2D LBM method is used to model an electron beam line melt. In this study individual randomly distributed particles are considered. Phenomena including wetting and capillary forces are included in the model. The electron beam is modeled as a Gaussian heat source. Wetting condition is numerically tested as well as process parameters. The impact of particle distribution is discussed. However, the thermal-capillary effect is neglected. In [6] the LBM simulations are extended to layer upon layer fabrication and consolidation mechanisms. In [10] a CFD simulation is performed to model a single line melt on a powder bed, comparing the effect of laser melt with and without surface tension. It is concluded that surface tension has a big impact on the melt flow dynamics. Here thermal-capillary effect is not included. The same author in [11] extends his laser model by the use of a ray tracing as well as adding thermo-capillary force and recoil pressure force to the model. The packing density of the particles in the simulation is fairly low.

In this project a state-of-the-art CFD multi-phase flow solver IPS IBOFlow, developed by Fraunhofer-Chalmers Centre for Industrial Mathematics (FCC), will be used to simulate the melt pool of the SLM process [12, 13]. IBOFlow has previously been used to successfully simulate a number of different industrial application, such as fiber suspension flow [14],[15], rotary bell spray simulation [16], and sealing application [17]. Including cases where surface tension play a pivotal role [18]. However, the surface tension was considered constant i.e. no varying surface tension and no tangential surface tension force has been simulated. To be able to more accurately capture the dynamics of the melt pool, the existing surface tension framework has been extended with a temperature dependent surface tension model and thermo-capillary surface tension force. The proposed improvements of the existing framework are assessed thoroughly and the new additions to the surface tension framework are evaluated and validated against analytic results. The improved and extended surface tension model is used in IBOFlow existing AM framework to simulate a single line melt of the SLM process.

1.2 Aim

The aim of this thesis is to evaluate and validate the improved and extended temperature dependent surface tension framework in IBOFlow. This is done in order to demonstrate a single line melt on a metal powder bed simulation where the surface tension force affect the motion of the liquid metal.

2

Additive Manufacturing

In this chapter a thorough description of the industrial relevant metal additive manufacturing technique selective laser melting is presented. This is followed by a section describing the physical phenomena occurring during selective laser melting.

2.1 Selective Laser Melting

Selective laser melting (SLM) is a metal AM technique based on using a laser to fully melt a selected part of a metal powder bed to manufacture 3D parts. When using SLM, new complex parts can be constructed which has previously not been possible due to the limitations of conventional manufacturing techniques. For example cellular structures, parts with internal structure or heat flux canals [19]. SLM is also considered most suitable for parts requiring unique configuration and which are produced in a small number of quantities. Example of such part are dental and medical devices, and low turnover replacement parts. Furthermore, metal AM is also suitable for parts where strength is a major concern such as machinery and aircraft. [20]. The advantage of SLM is that near fully dense component for functional use can be produced directly from a digital computer aided design (CAD) file, thus lowering the time-to-market substantially compared to conventional manufacturing techniques [3]. In the following section a SLM system is described. This is follow by a description of the process cycle and the process parameter of SLM. Lastly, common material of SLM process are presented.

2.1.1 Selective Laser Melting System

A SLM machine consists of a laser system, scanner system, building chamber and a powder storage chamber. In Figure 2.1 a typical SLM machine is depicted.

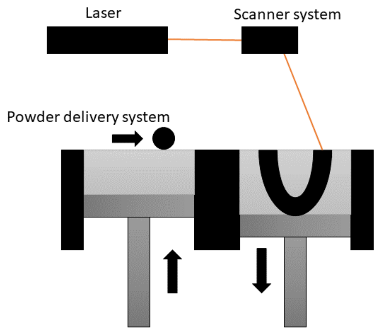

Figure 2.1: Depiction of a typical Selective Laser Melting machine

In Figure 2.1 the feeding material, i.e. the metal powder, is stored to the left in the powder storage chamber. On the right side a part is being fused together from metal powder inside the building chamber. Both the powder storage chamber and the building chamber are placed on top of vertically movable pistons. A powder delivery system, consisting of either a roller or a doctor blade, delivers the powder from the storage chamber to the building chamber and distributes the particles over a substrate. Above the building chamber a scanner system directs and guides the laser onto the powder filled substrate. In SLM, a solid state laser such as Nd:YAG or Yb:YAG laser is usually used; however, a CO_2 laser can be used as well. The fabrication takes place inside an enclosed chamber. This is because an inert gas is needed to reduce oxidation of the heated metal powder. The size of the part to be manufactured is limited by the size of the building chamber. [21]

2.1.2 Process cycle and Process parameters

At the start of a SLM process cycle a layer of metal powder is deposited on a substrate. Usually the powder particles are between $20 - 50\,\mu$m in diameter. Then a selected part of the metal powder is irradiated by a high powered laser so that the powder is heated up and in turn starts to melt. The laser moves rapidly back and forth in straight lines to scan a 2D selected area corresponding to a cut section of a 3D part. As the metal particles melt and liquefies they coalesce into a melt pool. When the heat source has passed, the melt pool cools down and solidifies to form the product. It is important that the current powder layer fuses together with the previous layer so that a 3D part can be formed from 2D cross sections. After the laser has completed the scan of the current layer, a piston lowers the substrate by one layer height. A new layer of powder is then distributed on top of the previous one. The process of melting and powder layer distribution is repeated until a three dimensional part is constructed. The powder loss is very low in SLM, and all unused powder, i.e. powder that has not been melted, is sieved and can be reused to create new parts from AM.

There are five building parameters which control the SLM process. These are powder layer height denoted H, laser scanning speed denoted V_L, laser power denoted P_L, laser spot size denoted D_L, and Hatch spacing. Hatch spacing refers to the space between two line melts. Today the impact of a specific combination of these process parameters on particular powder material are not fully understood and trial and error experiments has to be conducted in order to find the optimal process parameters. The process parameters directly affect the melt flow which in turn affect the mechanical properties of the constructed part [6]. Usually the scanning speed varies between 500-3500mm/s and the laser power ranges from 50-400W. The layer thickness is usually between 20-100μm [4]. All above parameters affect the porosity, layer connectivity and the surface roughness of the part being produced [6].

2.1.3 AM materials

Only a limited number of metals and alloys has been commercially used as powder for SLM. Among these are titanium alloys, nickel super alloys, aluminum, tool steel and stainless steel where the titanium alloy Ti-6Al-4V is being the one far most investigated [22]. Ti-6Al-4V or Ti64 is a common material in metal AM. Ti64 consist of of around 90 wt% titanium, 6 wt% aluminum and 4 wt% vanadium. Ti64 has a high specific strength which makes it useful for medical implants, turbine blades and aero engines [23]. Due to the rapid cooling occurring in metal AM dense fine grain microstructure is formed. This fine microstructure gives the Ti64 excellent material properties. The inert gas used in the building chamber is usually Argon (Ar). Helium can be used as well; however, Helium is more expensive.

2.2 Physical phenomena of SLM

During the SLM process several physical phenomena are present which influence the process stability and the quality of the finished part. As the laser irradiates the material the photon and electron energy is transformed into thermal energy by absorption. The laser is reflected at the particle surface allowing deep penetration into the particle bed and the substrate. During the intensive heating the material melts and forms a melt pool. Convection of the melt pool is driven by different external forces such as gravity, surface tension, the thermo-capillary effect and evaporation pressure. The thermo-capillary force is present due to the temperature dependant surface tension of liquid metals. The metals surface tension lowers with increasing temperature causing the thermo-capillary force to induce fluid motion away from the temperature peak in the center of the melt pool and thus increase the heat transport. Due to high melt pool temperatures the material evaporates and the resulting vapour pressure additionally drive the fluid motion. Heat transport such as thermal radiation, convection and evaporation cause heat loss of the melt pool. As the temperature of the melt pool decreases the material solidifies and forms the part. In Figure 2.2 an overview of the occurring physical phenomena are presented. [24]

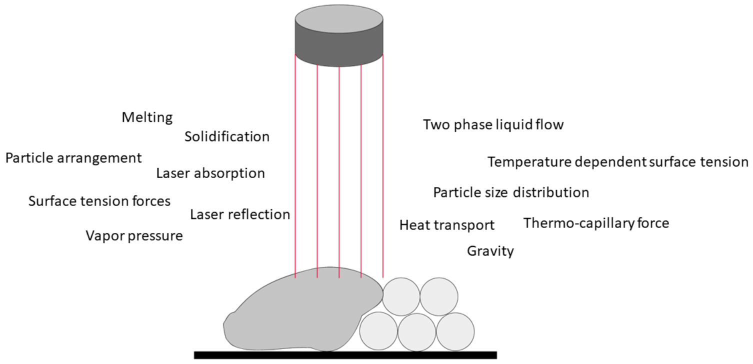
Melting
Solidification
Particle arrangement
Laser absorption
Surface tension forces
Laser reflection
Vapor pressure
Two phase liquid flow
Temperature dependent surface tension
Particle size distribution
Heat transport
Thermo-capillary force
Gravity

Figure 2.2: Physical phenomena as a laser melts a metal particle bed.

In order to simulate the melt flow these physical phenomena needs to be numerically modeled.

3

Surface Tension force balance

In this chapter the significance of the surface tension force on the melt flow is analyzed. This is done by considering relevant dimensionless groups. Following is a thorough derivation of the surface balance equation, including a description of both the normal and tangential component.

3.1 Dimensionless groups in metal AM

The flow of the melt pool in SLM is characterized using two dimensionless groups: the Bond number (Bo) and the Laplace number (La). The Bond number is defined as

$$Bo = \frac{\rho g L^2}{\sigma}, \tag{3.1}$$

where ρ is the density, g is the gravitational constant, L is the characteristic length and σ is the surface tension. The Bo number describes the ratio between the impact of the gravitational forces and surface tension forces on the flow. A high Bo number means that gravitational forces are dominant over surface tension forces while a low Bo number (usually less than unity) indicate the opposite. For metal AM, such as SLM, the density of the liquid metal is in the order of $10^3\,\mathrm{kg/m^3}$, the gravity is in the order of $10\,\mathrm{m/s^2}$ and the surface tension is in the order of $1\,\mathrm{N/m}$. The diameter D_p of the particles is chosen as the characteristic length, which is usually in the order of $10^{-4}\,\mathrm{m}$. This leads to:

$$Bo \approx 10^{-4}. \tag{3.2}$$

This means that surface tension forces are dominant compared to gravitational forces. The Laplace number is defined as

$$La = \frac{\sigma \rho L}{\mu^2}, \tag{3.3}$$

where μ is the dynamic viscosity. The La number describes the relation between the surface tension and the inertial forces to the viscous forces. A high La number means that surface tension and inertial forces are dominant over viscous force and a low La number (less than unity) indicate the opposite. In metal AM the dynamic viscosity of the liquid metal is usually in the order of 10^{-3} PaS. Together with the previously mentioned parameters, again the length scale L is set to diameter D_p, this yields a very high La number for metal particles, usually around:

$$La \approx 10^5. \tag{3.4}$$

This means that surface tension together and inertial forces are dominant over viscous forces. The La number and the Bo number together thus indicate that surface tension forces are dominant over gravitational and viscous forces in the melt flow during the SLM process.

3.2 Surface tension

The origin of the interfacial tension, also know as surface tension, between two fluids lies in different attractive inter-molecular forces. Consider a water molecule inside a bulk of water. The water molecule is surrounded by neighbour molecules which it feels mutual attraction with. A water molecule on the surface on the other hand is surrounded by a lesser amount of attractive neighbours and thus is in an energetically unfavorable state. The fluid will act to minimize its surface area since it is energetically costly to create new surface. The result is a energy area density that acts in all directions parallel to the surface. Surface tension σ has the unit energy per area or analogously force per unit length.

3.2.1 Derivation of surface force balance

Considering the fluid-fluid interface around a surface S as shown in Figure 3.1. This surface is bounded by a closed curve C with a surface unit normal $\mathbf{n}$ outward and $\hat{\mathbf{n}}$ inward, so that $\mathbf{n} = -\hat{\mathbf{n}}$. A force per unit length of magnitude σ at every point along this curve C acts in the S-direction to flatten the surface S. Performing a force balance on volume V over the interface S

$$\int_V \rho \frac{D\mathbf{u}}{Dt} dV = \int_V \mathbf{f} dV + \int_S [\mathbf{t(n)} + \hat{\mathbf{t}}(\hat{\mathbf{n}})] dS + \int_C \sigma \mathbf{s} dl. \tag{3.5}$$

The left hand side (LHS) represents the inertial force over the volume element dV. The first term on the right hand side (RHS) is the body force. The second term on the RHS denotes the surface forces where $\mathbf{t(n)} = \mathbf{n} \cdot \mathbf{T}$ is the hydrodynamic force exerted by the upper fluid on the interface and $\hat{\mathbf{t}}(\hat{\mathbf{n}}) = \hat{\mathbf{n}} \cdot \hat{\mathbf{T}}$ is the hydrodynamic force exerted by the opposite side, i.e. under the interface. The hydrodynamic forces act on a surface element dS. The last term on the RHS is the surface tension force acting along perimeter C where dl is an increment along the curve C.

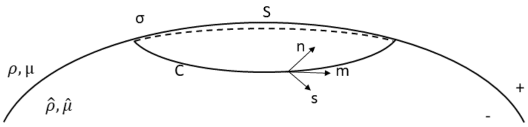

Figure 3.1: Fluid-fluid interface, ρ, μ belonging to upper surface (+) and $\hat{\rho}, \hat{\mu}$ belonging to lower surface (-).

Let ε be a length scale associated the fluid element V as in Figure 3.2. We see that the LHS and the first term on the RHS, i.e. the inertial force and the body force, scale with ε^3, the surface force scale with ε^2 and the line force scale with ε.

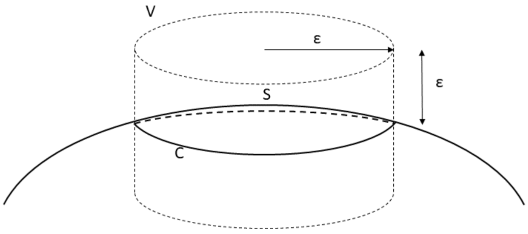

Figure 3.2: Control volume around the surface interface, where ε denote the length elements

As $\varepsilon \longrightarrow 0$ the inertial and the body force terms will disappear, so that

$$\int_S [\mathbf{t}(\mathbf{n}) + \hat{\mathbf{t}}(\hat{\mathbf{n}})] dS + \int_C \sigma \mathbf{s} dl = 0. \tag{3.6}$$

To further evaluate this expression we consider Stokes theorem for an arbitrary vector $\mathbf{F}$

$$\int_C \mathbf{F} \cdot \mathbf{m} dl = \int_S \mathbf{n} \cdot (\nabla \times \mathbf{F}) dS. \tag{3.7}$$

Let $\mathbf{F} = \mathbf{f} \times \mathbf{b}$, where $\mathbf{b}$ is an arbitrary constant vector. Substituting the new definition for $\mathbf{F}$ into the the expression above we get

$$\int_C (\mathbf{f} \times \mathbf{b}) \cdot \mathbf{m} dl = \int_S \mathbf{n} \cdot (\nabla \times (\mathbf{f} \times \mathbf{b})) dS. \tag{3.8}$$

Using two standard vector identities

$$(\mathbf{f} \times \mathbf{b}) \cdot \mathbf{m} = -\mathbf{b} \cdot (\mathbf{f} \times \mathbf{m}), \tag{3.9}$$

and

$$\nabla \times (\mathbf{f} \times \mathbf{b}) = \mathbf{f}(\nabla \cdot \mathbf{b}) - \mathbf{b}(\nabla \cdot \mathbf{f}) + \mathbf{b} \cdot \nabla\mathbf{f} - \mathbf{f} \cdot \nabla\mathbf{b} = -\mathbf{b}(\nabla \cdot \mathbf{f}) + \mathbf{b} \cdot \nabla\mathbf{f}. \tag{3.10}$$

Inserting into equation above we get

$$-\int_C \mathbf{b} \cdot (\mathbf{f} \times \mathbf{m})dl = \int_S \mathbf{n} \cdot (-\mathbf{b}(\nabla \cdot \mathbf{f}) + \mathbf{b} \cdot \nabla\mathbf{f})dS. \tag{3.11}$$

Since **b** is a constant vector we thus get

$$\mathbf{b} \cdot \int_C (\mathbf{f} \times \mathbf{m})dl = \mathbf{b} \cdot \int_S (\mathbf{n}(\nabla \cdot \mathbf{f}) - \mathbf{n} \cdot \nabla\mathbf{f})dS. \tag{3.12}$$

Since **b** is arbitrary it vanishes identically. We thus get

$$\int_C (\mathbf{f} \times \mathbf{m})dl = \int_S (\mathbf{n}(\nabla \cdot \mathbf{f}) - \mathbf{n} \cdot \nabla\mathbf{f})dS. \tag{3.13}$$

Now we choose $\mathbf{f} = \sigma\mathbf{n}$ and consider that $\mathbf{n} \times \mathbf{m} = -\mathbf{s}$. One ends up with

$$-\int_C \sigma\mathbf{s}dl = \int_S [\mathbf{n}\nabla \cdot (\sigma\mathbf{n}) - \nabla(\sigma\mathbf{n}) \cdot \mathbf{n}dS] = \int_S [\mathbf{n}\nabla\sigma \cdot \mathbf{n} + \sigma\mathbf{n}(\nabla \cdot \mathbf{n}) - \nabla\sigma - \sigma(\nabla\mathbf{n}) \cdot \mathbf{n}]dS. \tag{3.14}$$

We note that:

$\nabla\sigma \cdot \mathbf{n} = 0$ since $\nabla\sigma$ must be tangent to the surface S, and also that $(\nabla\mathbf{n}) \cdot \mathbf{n} = 0$.

Considering this the final result becomes

$$\int_C \sigma\mathbf{s}dl = \int_S \nabla\sigma - \sigma\mathbf{n}(\nabla \cdot \mathbf{n})dS. \tag{3.15}$$

In this expression we remove the part of the surface tension gradient that is normal to the surface and are thus left with the tangential gradient operator which is defined by

$$\nabla_s = [\mathbf{I} - \mathbf{nn}] \cdot \nabla. \tag{3.16}$$

This tangential gradient operator appears only because σ and $\mathbf{n}$ are only defined on the surface. Inserting equation 3.15 into equation 3.6 and replacing the expressions for the hydrodynamic forces with the ones above one ends up with the surface force balance equation

$$\int_S [\mathbf{n} \cdot \mathbf{T} + \hat{\mathbf{n}} \cdot (\hat{\mathbf{T}})]dS = \int_S \sigma\mathbf{n}(\nabla \cdot \mathbf{n}) - \nabla_s\sigma dS. \tag{3.17}$$

Since this equation is defined for an arbitrary fluid volume element the integrand must vanish identically. The local expression for the stress balance equation thus reads

$$\mathbf{n} \cdot \mathbf{T} - \mathbf{n} \cdot (\hat{\mathbf{T}}) = \sigma \mathbf{n}(\nabla \cdot \mathbf{n}) - \nabla_s \sigma, \tag{3.18}$$

where the terms on the LHS of the local surface force balance represent the difference in stress between the fluid on the upper part and the fluid on the lower part. The first term on the RHS, $\sigma \mathbf{n}(\nabla \cdot \mathbf{n})$ represent the normal curvature force per unit area associated with the local curvature of the interface. The second term on the RHS, $\nabla\sigma$ represent the tangential stress which is associated with the gradient in surface tension.

3.2.2 Normal force balance

We get the normal surface force balance on the interface by taking the scalar product of surface normal, $\mathbf{n}$, and equation (3.18). This yields

$$\mathbf{n} \cdot \mathbf{T} \cdot \mathbf{n} - \mathbf{n} \cdot (\hat{\mathbf{T}}) \cdot \mathbf{n} = \sigma\kappa = \mathbf{f}_\sigma^n, \tag{3.19}$$

where $\kappa = \nabla \cdot \mathbf{n}$ is the curvature. The LHS describes the jump in normal stress across the interfaces. The RHS describes the curvature force per unit area. These forces must balance across the interface. We note that if there is no curvature across the interface i.e $\kappa = \nabla \cdot \mathbf{n} = 0$ there is no jump in normal force between the two fluids.

3.2.3 Tangential force balance

The tangential surface force balance is obtained by taking the scalar product of any surface tangential vector, $\mathbf{t}$, and equation (3.18). This yields

$$\mathbf{n} \cdot \mathbf{T} \cdot \mathbf{t} - \mathbf{n} \cdot (\hat{\mathbf{T}}) \cdot \mathbf{t} = \nabla_s\sigma = \mathbf{f}_\sigma^t, \tag{3.20}$$

where the terms on the LHS describes the jump in the tangential component of the hydrodynamic stress across the interface of the two fluids. The RHS describes the gradient of the surfaces tension across the interface. If the surface tension is constant across the interface the RHS becomes zero. Since the LHS only include velocity gradients and no pressure, a constant surface tension will yield no motion of the boundary. A variation of surface tension across an interface can be caused by concentration gradient or by a temperature gradient. If the surface tension varies with temperature the tangential surface tension force may be referred to as the thermo-capillary force.

4

Modeling framework

In this chapter the governing transport equations which is solved for in IBOFlow is presented. This includes the Navier Stokes equation, the energy equation and volume of fluid (VOF) model which is used to model two phase flow. This is followed by a section about the solution procedure and discretization technique used in IBOFlow. Lastly a section about the AM modeling framework in IBOFlow is presented.

4.1 Governing equations

In this section the governing transport equations are described. These include the conservation of mass, conservation of momentum and conservation of energy. This section include a brief derivation and description of the governing equations, for further information see [25].

4.1.1 Conservation of Mass

The conservation of mass equation says that the mass in a system is preserved i.e. no mass is created or destroyed. It is further assumed that no mass sources or sinks exists in the system so that the mass in the system as well as of each phase is considered a conserved quantity. The conservation of mass is governed by the continuity equation, which can be expressed as

$$\frac{\partial \rho}{\partial t} + \nabla \cdot \rho \mathbf{u} = 0. \tag{4.1}$$

Where t is time, $\nabla \cdot$ is the divergence operator and $\mathbf{v}$ is the velocity vector. We assume that the flow is incompressible i.e the density in a fluid parcel is constant in time and space. The equation is thus reduced to

$$\nabla \cdot \mathbf{u} = 0. \tag{4.2}$$

Equation 4.2 above says that the divergence of the velocity is zero everywhere.

4.1.2 Conservation of Momentum

The balance of momentum is governed by the momentum equation which reads

$$\rho \frac{D\mathbf{u}}{Dt} = \nabla \cdot \boldsymbol{\sigma} + \mathbf{f}, \tag{4.3}$$

where $\boldsymbol{\sigma}$ is the stress tensor and $\mathbf{f}$ is the body force. The fluid is considred Newtonian so that the stress tensor is the sum of the pressure p$\mathbf{I}$, and the viscous stress tensor $\boldsymbol{\tau}$. Writing out the material time derivative on the LHS, applying the continuity equation and the product rule results in the conservative form of the momentum balance

$$\frac{\partial \rho \mathbf{u}}{\partial t} + \nabla \cdot (\rho \mathbf{u}\mathbf{u}) = -\nabla p + \nabla \cdot \boldsymbol{\tau} + \mathbf{f}. \tag{4.4}$$

The viscous stress tensor is modelled as a linear relation of the strain rate tensor $\mathbf{E}$. We get the constitutive relation:

$$\boldsymbol{\tau} = 2\mu \mathbf{S}. \tag{4.5}$$

Where the rate of strain tensor is defined as

$$\mathbf{S} = \frac{1}{2}(\nabla \mathbf{u} + \nabla \mathbf{u}^T). \tag{4.6}$$

We finally end up with:

$$\frac{\partial \rho \mathbf{u}}{\partial t} + \nabla \cdot (\rho \mathbf{u}\mathbf{u}) = -\nabla p + \nabla \cdot (\mu(\nabla \mathbf{u} + \nabla \mathbf{u}^T)) + \mathbf{f}. \tag{4.7}$$

Equation 4.7, and also sometimes together with equation 4.2, are referred to as the Navier-Stokes equations, which describe the relation between the fluid velocity, pressure and the applied forces on a system. The flow is considered laminar so no turbulence models are necessary.

The body forces consider in this problem are gravity, $\mathbf{f}_g$ and the surface tension force $\mathbf{f}_\sigma$ so that:

$$\mathbf{f} = \mathbf{f}_g + \mathbf{f}_\sigma. \tag{4.8}$$

Although the surface tension force acts only on the interface between two fluids it is usually modeled as a body force. This will be discussed further in the section 4.4.4. The gravity force is expressed through the Boussinesq approximation

$$\mathbf{f}_g = \rho_0 \mathbf{g} \beta (T - T_0) + \mathbf{g}, \tag{4.9}$$

where T is the temperature, ρ_0 is the density at the reference temperature T_0, $\mathbf{g}$ is the gravity and β is the volume expansion coefficient.

4.1.3 Conservation of Energy

The energy equation balances energy inside the system with the energy that enters or leaves the system. The energy equation, without radiation, reads

$$\rho\frac{De}{Dt} = \boldsymbol{\sigma}^T\nabla\mathbf{u} - \nabla\cdot\mathbf{q} + \mathbf{q}_{ext}, \tag{4.10}$$

where e is the internal energy, $\mathbf{q}$ denotes the conductive heat transfer and $\mathbf{q}_{ext}$ denotes the external heat source. We apply Fouriers law to the heat transfer

$$\mathbf{q} = -k\nabla T, \tag{4.11}$$

where k is he heat conductivity, which is constant in our case. Since the flow is considered incompressible the internal energy can be related to the temperature as

$$de = c_p dT, \tag{4.12}$$

where c_p is the heat capacity. Further, we assume that there is no dissipation. This assumption is possible since the fluid is a common liquid (i.e. not an lubricant oil) [25]. This results in

$$\frac{DT}{Dt} = a\nabla^2 T + \frac{\mathbf{q}_{ext}}{\rho c_p}, \tag{4.13}$$

where $a = \frac{k}{\rho c_p}$ is the thermal diffusivity. Applying the material time derivative on the LHS we end up with

$$\frac{\partial T}{\partial t} + \mathbf{v}\cdot\nabla T = a\nabla^2 T + \frac{\mathbf{q}_{ext}}{\rho c_p}. \tag{4.14}$$

4.1.4 Volume of Fluid

The volume of fluid (VOF) [26] method is used to model two phase flow. In the VOF method a volume fraction function α is introduced. The volume fraction is defined as

$$\alpha = \frac{\text{Volume of liquid in control volume}}{\text{Total volume of the control volume}}. \tag{4.15}$$

The control volume during the numerical simulations is a computational cell. This means that for cells in the lighter fluid phase α is unity and in the heavier phase α is zero. Cells with a value of α between zero and one must contain the fluid-fluid interface region between the two phases

$$\alpha = \begin{cases} 0, & \text{in heavier fluid} \\ 0 < \alpha < 1, & \text{in cells containing the interface} \\ 1, & \text{in lighter fluid.} \end{cases} \tag{4.16}$$

In the VOF method only a single momentum equation is being solved for the two phases. The material properties are updated through a linear interpolation between the two phases

$$\phi = \alpha\phi_l + (\alpha - 1)\phi_g, \tag{4.17}$$

where ϕ is denoted a various material property. The volume fraction α and thus also the fluid-fluid interface is advected through the material time derivative

$$\frac{D\alpha}{Dt} = \frac{\partial\alpha}{\partial t} + \mathbf{v} \cdot \nabla\alpha = 0. \tag{4.18}$$

The location of the interface can be used to set boundary conditions, such as the surface tension. When solving this equation it is important to retain a low amount of numerical diffusion otherwise the boundary will smear out and the interface will lose its definition. This will be discussed further in the section 4.3. The VOF method is a cheap method in turns of memory and since it follows regions instead of surfaces all problem associated with intersecting surface are avoided.

4.2 Numerical solution procedure

IBOFlow is a finite volume based solver for incompressible multiphase flow. Navier Stokes equations, equation (4.2) and (4.7), the transport equation for temperature (4.14) together with the equation of the volume fraction advection (4.18) are solved in IBOFlow. The equations are discretized on a Cartesian octree grid which can dynamically be refined and coarsened the enhance or reduce the resolution of the flow if necessary. This is convenient in flows which require a refined mesh at local areas such as the interface between two fluids.

A sequential solution method is employed in IBOFlow. At the beginning of each time step the Navier-Stokes equations are solved first. Afterwards the temperature equation (4.14) and the volume fraction advection equation (4.18) is solved. Equation (4.17) is then used to update the density and viscosity in each computational cell.

The Navier Stokes equations are solved numerically using the SIMPLEC method. SIMPLEC is a pressure projection method. SIMPLEC stands for Semi-Implicit Method for Pressure Linked Equations-Consistent. The SIMPLEC algorithm is a segregated solution technique which first approximates the momentum equation with an estimated pressure field and then corrects the pressure by employing the continuity equation. Applying the pressure field to the previous velocity field results in a velocity field which satisfies the continuity equation. The method is an iterative method which iterate until the pressure correction term is very small. The results are a velocity and pressure field that satisfy the momentum and continuity equations.

All the variables are stored in a co-located grid arrangement. To prevent pressure oscillation a pressure-weighted flux interpolation by Rhie and Chow [27] is used. An implicit Euler scheme is used for the temporal discretization of the unsteady term in all transport equations.

4.3 Volume fraction advection model

In order to predict the position of the interface accurately and maintain a sharp interface the volume fraction advection equation must be discretized and solved for. However this equation is prone to problems with the advection of a step function, namely how to advect the interface without diffusing, dispersing or wrinkling it. IBOFlow uses Compressive Interface Capturing Scheme for Arbitrary Meshes (CICSAM) [28] to numerically solve the volume fraction equation.

CICSAM uses a finite volume discretization based on integral of equation (4.18). The Crank-Nicolson scheme is used as temporal discretization, which makes it second order accurate in time. This is also necessary if operator splitting is to be avoided and if the solution is to be as free as possible from numerical diffusion in all flow directions.

Depending on the direction of the flow CICSAM uses a smooth blending of ULTIMATE-QUICKEST, which perserves interface best, and HYPER-C , which is the most compressive differencing scheme. The CICSAM techniques is based on the concept of normalized variable diagram (NVD) togheter with the convection boundedness criterion (CBC). Furthermore, an additional courant number restriction is used to limit the upper bound of the CBC region. The CICSAM technique preserves boundedness over the scalar field. This means that as the scalar field is convected cell values are limited to $0 \leqslant \alpha \leqslant 1$.

4.4 AM framework

In this section the AM modeling framework is presented. This include a laser model, material models, phase change model, and the surface tension model used.

4.4.1 Laser model

The laser is modeled using a ray tracing algorithm were circular pattern of rays are directed from an applicator position to the substrate. The rays deposit energy to the computational cells based on the phase of the cell, more energy is deposited onto the heavier phase, and depth of the cell, more energy is deposited closer to the surface of the VOF. This implementation of energy deposition allows for shadowing, which occurs when particles block the rays from hitting the substrate, and partial melting of particles.

4.4.2 Material models

The following material models are used to model the temperature dependent material properties. The viscosity of the heavier fluid decreases with increasing temperature. This is modeled with the Arrhenius equation.

$$\ln \mu = \ln \mu_0 + \frac{\Delta E_a}{R} T^{-1}, \tag{4.19}$$

where ΔE_a is the activion energy, R the universal gas constant and μ_0 the nominal dynamic viscosity.

The specific heat capacity, denoted c_p, of heavier fluid is dependent if the local cell is in phase transformation of not. If the fluid cell is solid or liquid the heat capacity is constant and if the fluid cell is between the melting temperature and the liquidus temperature the latent heat is added to the heat capacity according to

$$\tilde{c}_p = \begin{cases} c_p, & T > T_l \\ c_p + \frac{L}{T_l - T_m}, & T_m < T < T_l, \\ c_p, & T < T_m. \end{cases} \tag{4.20}$$

4.4.3 Phase change model

During the SLM process described in section 2.1 the metal is heated to its melting temperature so that it melts and liquefies. Later during the SLM process the heat source is removed and the liquid metal cools down and solidifies. In order for the solid to become liquid and the liquid to become a solid, a phase change model is needed. The phase change in IBOFlow is modeled using latent temperature. Two different temperatures are of importance, the melting temperature T_m and the liquidus temperature T_l. Initially the metal is in a solid state. In the solid state the velocity is set to zero. As the solid is heated up it remains a solid until its temperature reaches T_l. When the temperature reaches T_l the metal becomes a liquid. The movement of the liquid is governed by the Navier Stokes equations.

When the heat source is removed the temperature lowers locally as the heat is advected and diffuses. When the temperature of the liquid reaches T_m the metal solidifies and the velocity is set to zero. During the phase change the heat capacity of the local melting cell is governed by equation (4.20).

4.4.4 Surface tension model

The current surface tension framework in IBOFlow and the problems associated with it is presented in this section. In this surface tension framework only normal component of the surface tension force described in section 3.2 is modeled. The surface tension framework is based on the continuum surface force method by Brackbill et al [29]. The model equation reads

$$\mathbf{f}_\sigma = \mathbf{f}_\sigma^n = \sigma\kappa\mathbf{n}\delta, \tag{4.21}$$

where κ is the curvature of the liquid-gas interface and δ is the kronecker delta indicating that the surface tension is only active on the interface. As mentioned in section 4.1.2 the surface force is modeled as a body force; however, it should only act on the interface surface. This is resolved by setting $\delta = |\nabla\alpha|$ which makes the force only present on the interface surface. Further more, the unit normal is given by

$$\mathbf{n} = \frac{\nabla\alpha}{|\nabla\alpha|}. \tag{4.22}$$

This simplifies the expression for the surface tension force to

$$\mathbf{f}_\sigma = \sigma\kappa\nabla\alpha, \tag{4.23}$$

where the gradient of the volume fraction, $\nabla\alpha$ is the normal of the VOF interface. Currently the curvature is calculated according to

$$\kappa = \nabla\cdot\mathbf{n} = \nabla\cdot\frac{\nabla\alpha}{|\nabla\alpha|}. \tag{4.24}$$

When discretizing and calculating the curvature problems arise. While wanting the interface to remain sharp and also taking the second derivative of the volume fraction field the result will not be a smooth field. Thus resulting in local variations in the surface tension force. These local variations cause an imbalance with the associated pressure gradient which will create artificial velocity fields. These artificial velocity fields are non existing in the actual flow. The artificial currents can propagate and grow in magnitude which can cause the interface to deform and in turn break up. Because of these artificial velocities are often referred to as parasitic or spurious currents. These spurious currents are a result of using the CSF method when applying the surface tension force on a co-located grid since there will be a mismatch between the pressure gradient and the applied force.

Laplacian smoothing of the volume fraction at the interface is applied to reduce the artificial velocities. The Laplacian smoothing operation on a uniform grid reads

$$\bar{\alpha}_i = \frac{1}{N}\sum_{j=1}^{N}\frac{\alpha_i + \alpha_j}{2}. \tag{4.25}$$

where $\bar{\alpha}_i$ is the new smoothed volume fraction, α_i is the old volume fraction in the current cell, α_j is the old volume fraction in the neighbour cell and N is the number of neighbour cells. The smoothed volume fraction is only used to calculating the interface normal, $\nabla\alpha$, and the curvature, κ, of the surface tension equation at the current time step. The Laplacian smoothed $\bar{\alpha}$ is not used to convect the volume fraction field and will not be stored. The Laplacian smoothing operation smooths the volume fraction so that a more even interface is produced and artificial currents are reduced. However, Laplacian smoothing leads to a wide location for where the surface tension force is applied.

4.4.5 AM Modeling limitations

In order to reduce computational cost and considering the limitations of the current computational frame work only physical phenomena of the largest impact on the melt flow dynamics are considered. No reflections of the laser rays will be modeled as this requires an extremely fine mesh which in turn increase the computational cost. Ejected particles during at the laser melt, which has been observed during experimental studies [30], will not be modeled. The particles in the simulation will be fixed in space during the simulation since the current computational frame work does not support CFD and DEM coupling.

5

Improvements to the Surface Tension Framework

In this chapter the steps taken to reduced the magnitude of the artificial velocities generated at interface as mentioned in section 4.4.4 are presented. This include a method for interfacial smoothing and height functions. Thereafter, a temperature dependent surface tension material model is presented together with the tangential surface tension force. These improvements and additions will be analyzed and validated in chapter 6 and 7

5.1 Interfacial Smoothing

The normal component of the surface tension force is modeled according as

$$\mathbf{f}_\sigma^n = \sigma \kappa \nabla \alpha. \tag{5.1}$$

The interface normal or $\nabla\alpha$ directly affect the magnitude, and direction the surface tension force. If the direction of the interface normal can be better approximated a more accurate normal surface tension force can be achieved. Furthermore $\nabla\alpha$ also affect location of where the normal surface tension force is applied. If a computational cell has a $\nabla\alpha$ value of zero, then there is no surface tension active in this cell. Thus can $\nabla\alpha$ be seen as a marker for where the interface is located and the normal surface tension is applied.

Laplacian smoothing of the volume fraction, α, at the interface results in a more accurate direction of the interface normal, $\nabla\alpha$; however, the interface where the normal surface tension force is applied gets diffuse and wide. Applying the Laplacian smoothing operator a second time to an already smoothed α results in further better approximation of the direction of $\nabla\alpha$; however, also an even more diffuse interface. IBOFlow has up until now only used the Laplacian smoothing operator once to smooth the α at the interface. A technique where Laplacian smoothing is applied ten times to the interface to even further improve the direction of $\nabla\alpha$ is proposed. The direction of the inwards interface normal from a ten times smoothed alpha is compared to the direction of the interface normal from an unsmoothed alpha on a sphere in Figure 5.1. For a sphere, the analytical inwards normal points towards the center of the sphere.

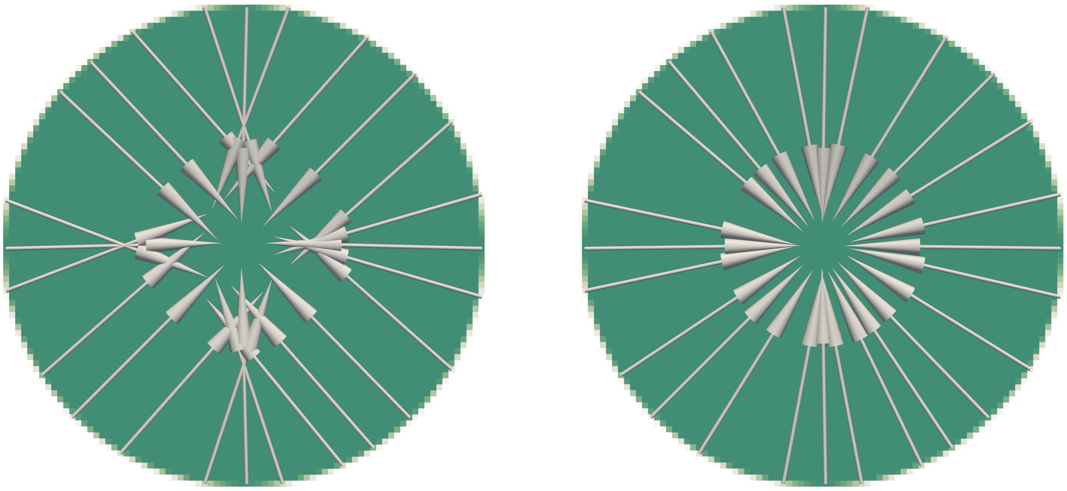

(a) Unsmoothed $\nabla\alpha$. **(b)** Laplacian smoothing 10 times $\nabla\bar{\alpha}$.

Figure 5.1: Inwards normal of the interface of a circle.

This $\nabla\bar{\alpha}$ has a more correct direction, normal to the interface; however, the interface will be very diffuse causing the normal surface tension force to be active on a wide amount of cells at the interface. To sharpen the interface where the normal surface tension force is active the ten times smoothed $\nabla\bar{\alpha}$ is normalized with the unsmoothed gradient of alpha. This is done by $\nabla\bar{\alpha}$ multiplied with the magnitude of the unsmoothed gradient of alpha $|\nabla\alpha|$ over the magnitude of the smoothed gradient of alpha $|\nabla\bar{\alpha}|$. This normalization procedure reads

$$\nabla\tilde{\alpha} = \nabla\bar{\alpha}\frac{|\nabla\alpha|}{|\nabla\bar{\alpha}|} \tag{5.2}$$

where the $\nabla\tilde{\alpha}$ is the improved normal which has been smoothed ten times and then normalized with the unsmoothed volume fraction gradient. With this normalization procedure, a computational cell where the magnitude of the surface tension force was zero before the Laplacian smoothing will again be zero. A sharp interface where the surface tension force is active has been achieved. A conservative normal surface tension force has also been attained with this normalization technique. The Laplacian smoothed and scaled volume fraction is only used in the calculation of a smooth volume fraction gradient $\nabla\tilde{\alpha}$, all other calculations are from the non-diffuse volume fraction.

5.2 Height functions

In order to reduce spurious currents around the VOF edge the height function technique is proposed [31][32][33]. The height function method is a technique for calculating interface normals and curvatures. Heights are calculated by summation of fluid volume fraction in the direction most normal to the VOF interface. The direction most normal to the surface is determined by

$$n_{max} = \max(n_x, n_y, n_z). \tag{5.3}$$

The normal is originally determined by the volume fraction gradient

$$\mathbf{n} = (n_x, n_y, n_z) = \nabla\alpha. \tag{5.4}$$

Choosing the right direction to sum the volume fraction is important and not trivial for highly inclined surfaces, in which the magnitude of all three normal components can be very similar. Therefore, the improved interface normal proposed in the previous section is used

$$\mathbf{n} = \nabla\tilde{\alpha}. \tag{5.5}$$

In 2D the height function summation is done according to a 7x3 stencil, for example if the direction most normal to the interface is $|n_y| > |n_x|$:

$$H_i = \sum_{t=j-3}^{j+3} \alpha_{i,t}\Delta, \tag{5.6}$$

where Δ is the grid size. A 2D example on how the height functions are calculated can be seen in Figure 5.2.

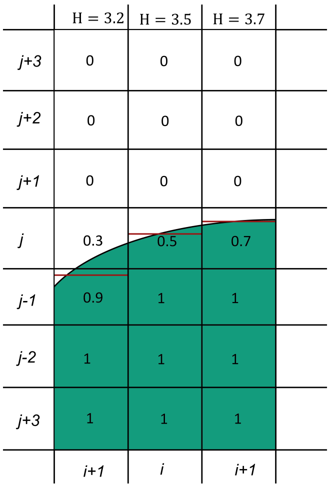

	H = 3.2	H = 3.5	H = 3.7
j+3	0	0	0
j+2	0	0	0
j+1	0	0	0
j	0.3	0.5	0.7
j-1	0.9	1	1
j-2	1	1	1
j+3	1	1	1
	i+1	*i*	*i+1*

Figure 5.2: Height function summation at VOF interface (2D)

In 3D the summation is done according to a 7x3x3 stencil. For example if the direction most normal to the interface is $|n_z| > |n_x|, |n_y|$:

$$H_{r,s} = \sum_{t=-t_{down}}^{t_{up}} \alpha_{i+r,j+s,k+t}\Delta, \tag{5.7}$$

for $r = -1, 0, 1$ and $s = -1, 0, 1$. These heights are then used to calculate the interface curvature κ.

5.2.1 Curvature calculation in 2D

In 2D if the curvature is calculated in the x-direction according to

$$\kappa_{2D} = \frac{H_{xx}}{(1 + H_x^2)^{3/2}}, \tag{5.8}$$

where the the partial derivatives H_x and H_{xx} are discretized using second order-central differences according to

$$H_x = \frac{H_{i+1} - H_{i-1}}{2\Delta}, \tag{5.9}$$

and

$$H_{xx} = \frac{H_{i+1} - 2H_i + H_{i-1}}{\Delta^2}. \tag{5.10}$$

5.2.2 Curvature calculation in 3D

In 3D the curvature is calculated according to

$$\kappa_{3D} = \frac{H_{xx} + H_{yy} + H_{xx}H_y^2 + H_{yy}H_x^2 - 2H_{xy}H_xH_y}{(1 + H_x^2 + H_y^2)^{3/2}}. \tag{5.11}$$

In 3D, a "smoother" parameter γ is introduced to improve the accuracy of the interface curvature computation [32]. The smoother parameter acts to smooth the first and second partial derivative of H when the angle formed between the height function direction and the interface normal vector, $\theta = \arccos\left[\max(|n_x|, |n_y|, |n_z|)\right]$ reaches a critical value. The derivatives are calculated as

$$H_x = \frac{\gamma(H_{1,1} - H_{-1,1}) + H_{1,0} - H_{-1,0} + \gamma(H_{1,-1} - H_{-1,-1})}{2\Delta(1 + 2\gamma)}, \tag{5.12}$$

$$H_{xx} = \frac{\gamma(H_{1,1} - 2H_{0,1} + H_{-1,1}) + H_{1,0} - 2H_{0,0} + H_{-1,0} + \gamma(H_{1,-1} - 2H_{0,-1} + H_{-1,-1})}{\Delta^2(1 + 2\gamma)}, \tag{5.13}$$

and

$$H_{xy} = \frac{H_{1,1} - H_{1,-1} - H_{-1,1} + H_{-1,-1}}{4\Delta^2}. \tag{5.14}$$

Where the smoother parameter γ is defined as

$$\gamma = \begin{cases} 0.2 & \text{if } \theta > \theta_{\text{critical}} \\ 0, & \text{otherwise,} \end{cases} \tag{5.15}$$

with the critical angle chosen as $\theta_{\text{critical}} = 0.8\,\text{rad}$. The smoothing procedure involves six nodes for H_x and nine nodes for H_{xx} in the curvature stencil instead of two and three nodes used when $\gamma = 0$. When $\gamma = 0$ the equations above produces a standard second-order finite difference approximation. The values of the smoother parameter and the critical angle has been taken from [32]. Furthermore, the smoother parameter can only be applied in 3D, for which precisely the curvature errors for highly inclined interface are larger.

5.3 Temperature dependent surface tension

The surface tension of the liquid metals vary with temperature [23],[34]. This is modeled according to the Eötvös rule, which states that surface tension is a linear function of the temperature. The temperature dependent surface tension equation reads

$$\sigma(T) = \sigma_0 + \sigma_T(T - T_l), \tag{5.16}$$

where the variables σ_0, σ_T and T_l are material specific parameter for the nominal surface tension, the surface tension temperature gradient and the liquids temperature, respectively. The local cell temperature T is obtained from the energy equation. The temperature dependent surface tension model is only present at the interface between the two fluids.

5.4 Tangential surface force

With a varying surface tension across the interface the tangential component of the surface tension becomes non zero. This force component is derived in section 3.2. The tangential component of the surface tension force is only active on the interface between the two fluids. In order to achieve this a Kronecker delta, δ, term needs to be added. The equation now reads

$$\mathbf{f}_\sigma^t = \nabla_s \sigma \delta, \tag{5.17}$$

where $\delta = |\nabla \alpha|$. The tangential surface tension force term is evaluated by knowledge of the local surface tension at each cell and using finite difference to evaluate the surface gradient, ∇_s, of the surface tension. This term is added to the normal component of the surface tension so that the surface balance equation is complete

$$\mathbf{f}_\sigma = \mathbf{f}_\sigma^n + \mathbf{f}_\sigma^t = \sigma\kappa\nabla\alpha + \nabla_s\sigma|\nabla\alpha|. \tag{5.18}$$

6

Simulations

In the following chapter validation cases are presented for the improvements and additions to the surface tension framework in IBOFlow. The improvements of the framework, the smoothed interface normal and the height functions, are evaluated and validated using a static droplet in equilibrium. The temperature dependent surface tension together with the tangential surface tension is validated against a thermo-capillary flow in a cavity. The validation of the new surface tension model has been performed with spatial and temporal convergence studies. Finally a single line melt simulation using the extended surface tension framework is performed to model the melt pool dynamics during the SLM process.

6.1 Static droplet in equilibrium

A smoothing and scaling procedure is used to improve the direction of the interface normal, and height functions has been employed in order to better approximate the curvature of the interface. In order to evaluated these proposed improvements, 2D and 3D simulations of a static droplet in equilibrium has been performed [35]. The static droplet in equilibrium case a droplet is placed at the center of a domain and the simulation setup can be seen in Figure 6.1.

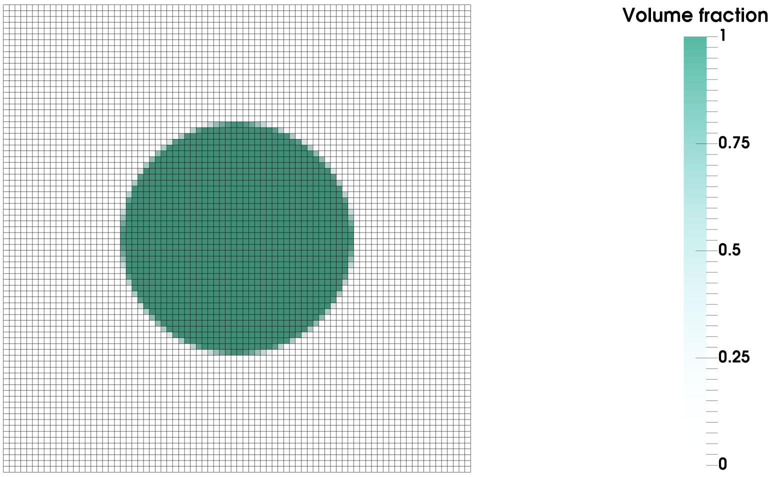

Figure 6.1: Static droplet in equilibrium.

No outer forces are active, i.e. the gravity is set to zero. For the equilibrium condition to be fulfilled the droplet should remain still and the interface should not move. If there exist any numerical imbalances the balancing forces will cause artificial velocities around the droplet thus breaking the equilibrium condition. Therefore, it is important to numerically solve the balance forces accurately. For this case the exact analytical pressure jump across the drop is given by

$$\Delta p_{exact} = \sigma \kappa, \tag{6.1}$$

and the analytic expression for the curvature is given by

$$\kappa_{exact} = \begin{cases} 1/R & \text{in 2D,} \\ 2/R & \text{in 3D.} \end{cases} \tag{6.2}$$

The drop is positioned at the center of a computational rectangular (2D) or cubic (3D) domain with side lengths of 8 m. The radius of the drop is set to $R = 2\,\mathrm{m}$ and the surface tension is set to a constant value of $\sigma = 73\,\mathrm{N/m}$. This resembles an up-scaled water droplet placed in air. The density inside the drop is $\rho_1 = 1\,\mathrm{kg/m^3}$ and the density of the outer phase ρ_2 is varied from 1 to $10^{-4}\,\mathrm{kg/m^2}$. The viscosity inside the drop is set to, $\mu_1 = 0.01\,\mathrm{Pas}$ and outside $\mu_2 = 0.001\,\mathrm{Pas}$. The velocity boundary conditions are free-slip. The simulations is performed on a uniform mesh where $\Delta x = \Delta y = h$ with mesh resolution $R/h = 5, 10, 20$ and, 40.

In order to evaluate the result the following L error norm calculations were performed

$$L_1(x) = \frac{\Sigma_{n=1}^{N}|x|}{N}, \tag{6.3}$$

and

$$L_{\inf}(x) = |x|_{max} = \max(x), \tag{6.4}$$

where x is either the velocity field $\mathbf{u}$ or the normalized curvature error κ_{error} which is defined as

$$\kappa_{error} = \frac{|\kappa - \kappa_{exact}|}{\kappa_{exact}}. \tag{6.5}$$

6.1.1 2D curvature evaluation

Four different calculations of the curvature are compared in the 2D simulations of the static droplet in equilibrium. These methods are presented below.

Regular curvature

In the first method the curvature is calculated using the original or regular formulation presented in section 4.4.4,

$$\kappa = \nabla \cdot \frac{\nabla\alpha}{|\nabla\alpha|}. \tag{6.6}$$

Regular curvature with improved normal

In the second method the curvature is calculated using the regular formulation but now the improved normal is now used instead so that

$$\kappa = \nabla \cdot \frac{\nabla\tilde{\alpha}}{|\nabla\tilde{\alpha}|}, \tag{6.7}$$

where $\tilde{\alpha}$ is smoothed using Laplacian smoothing and scaled.

Height function

In the third method height functions are used according to equation (5.8) in order to calculate the curvature. The direction in which the height functions summation stencil is calculated is determined by the normal direction calculated from the regular volume fraction, $\nabla\alpha$.

Height functions with improved normal

In the fourth method height functions are used again according to equation (5.8). However, this time the direction in which the height function summation stencil is calculated is determined by the improved normal, $\nabla\tilde{\alpha}$. A summary of the curvature estimation techniques can be seen in 6.1.

Table 6.1: VOF interface curvature estimation 2D

Method (Short name)	Normal $\mathbf{n}$	Curvature κ	Note
$\nabla\alpha$	-	$\nabla\cdot\frac{\nabla\alpha}{\lvert\nabla\alpha\rvert}$	Regular normal
$\nabla\tilde{\alpha}$	-	$\nabla\cdot\frac{\nabla\tilde{\alpha}}{\lvert\nabla\tilde{\alpha}\rvert}$	Improved normal
HF	$\frac{\nabla\alpha}{\lvert\nabla\alpha\rvert}$	HF	Regular normal
HF - $\nabla\tilde{\alpha}$	$\frac{\nabla\tilde{\alpha}}{\lvert\nabla\tilde{\alpha}\rvert}$	HF	Improved normal

In order to evaluate the different curvature calculation techniques in 2D several measures are considered, all of which are performed using the static droplet in equilibrium case. These measures include a mesh study, density ratio study, and a pressure evaluation study. The results of these studies are presented in section 7.1.1.

The mesh study is performed in order to investigate how the L_1 and L_{inf} error norms of the curvature are affected by the mesh size. In this mesh study the height function with smoothed interface normal $\nabla\tilde{\alpha}$ is not included.

The 2D curvature evaluation is continued with a density ratio study. In this density ratio study the L_1 and L_{inf} error norms of the velocity field are evaluated for three different density ratios of $\frac{\rho_2}{\rho_1} = 1$, $\frac{\rho_2}{\rho_1} = 10^2$, and $\frac{\rho_2}{\rho_1} = 10^4$. This evaluation is performed in order to investigate how the spurious currents around the VOF edge are affected by high density ratios commonly occurring in liquid metal and gas flows such as in metal AM.

Lastly the pressure is evaluated across a line over the domain. The pressure from the different numerical curvature procedures are compared to the exact pressure (6.1) in order to evaluate the performance of the different methods.

6.1.2 3D curvature evaluation

To evaluate the curvature in 3D, interface curvature calculations using five different curvature estimation techniques are considered.

Regular curvature

In the first method the curvature is calculated using the regular formulation presented in section 4.4.4

$$\kappa = \nabla\cdot\frac{\nabla\alpha}{|\nabla\alpha|}. \tag{6.8}$$

Regular curvature with improved normal

In the second method the curvature is calculated using the regular formulation but now the improved normal is now used where $\tilde{\alpha}$ is smoothed using Laplacian smoothing and scaling is applied to sharpen the location. The curvature is calculated as

$$\kappa = \nabla \cdot \frac{\nabla \tilde{\alpha}}{|\nabla \tilde{\alpha}|}. \tag{6.9}$$

Height function

In the third method height functions are used according to equation (5.11) to calculate the curvature. The direction in which the height functions summation stencil is calculated is determined by the normal direction calculated from the regular volume fraction, $\nabla \alpha$. In this method the smoother parameter, γ, described in equation (5.15) is set to zero such that the partial derivatives of the height functions are calculated using standard second order central difference scheme.

Height function, γ

In the fourth method height functions are used again according to equation (5.11) to estimate the curvature. The direction in which the height functions summation stencil is employed is determined by the normal direction calculated from the regular volume fraction, $\nabla \alpha$. However, this time the smoother parameter, γ, is used when calculating the partial derivatives of the height functions.

Height functions, γ, with improved normal

In the fifth method height functions are also again used according to equation (5.11). The smoother parameter, γ, is used when calculating the partial derivatives of the height functions. However, now the direction in which the height function summation stencil is calculated is determined by the improved normal, $\nabla \tilde{\alpha}$. This technique for calculating the curvature improves the direction in which the stencil for the height function is laid out. A summary of the curvature estimation techniques can be seen in 6.2.

Table 6.2: VOF interface curvature estimation

Method (Short name)	Normal $\mathbf{n}$	Curvature κ	Note
$\nabla \alpha$	-	$\nabla \cdot \frac{\nabla \alpha}{\lvert\nabla \alpha\rvert}$	Regular normal
$\nabla \tilde{\alpha}$	-	$\nabla \cdot \frac{\nabla \tilde{\alpha}}{\lvert\nabla \tilde{\alpha}\rvert}$	Improved normal
HF	$\frac{\nabla \alpha}{\lvert\nabla \alpha\rvert}$	HF	Regular normal, $\gamma = 0$
HF - γ	$\frac{\nabla \alpha}{\lvert\nabla \alpha\rvert}$	HF	Regular normal
HF - γ - $\nabla \tilde{\alpha}$	$\frac{\nabla \tilde{\alpha}}{\lvert\nabla \tilde{\alpha}\rvert}$	HF	Improved normal

Multiple measures are considered in order to evaluate the different curvature estimation techniques in 3D, all of which are performed using the static droplet in equilibrium. As with the 2D evaluation a mesh study, density ratio study, and a pressure evaluation comparison is performed. On top of this the curvature error and the velocity vectors are plotted on the surface of the 3D sphere. The results are presented in section 7.1.2.

The mesh study, density ratio study, and the pressure evaluation in 3D are performed in the same manner as in the 2D evaluation. The visualization of the curvature error κ_{error} and velocity vectors are on top of the 3D droplets surface is done in order to visualize at what location the magnitude of the error occur and how the magnitude of the error and its location is altered using different curvature calculation techniques.

6.2 Tangential surface tension force validation

In order to validate the temperature dependent surface tension and the tangential surface tension force a steady 2D thermo-capillary cavity flow is considered. The geometric setup with thermal boundary conditions can be seen in Figure 6.2. Initially a fluid fills the cavity up to a height of $h = 0.2\,\mathrm{m}$. The velocity boundary condition at the cavity walls are set to slip and the top is set to open. This case has been extensively tested in literature in both 2D and 3D, with and without gravity component included [36],[37],[38]. An asymptotic analytic solution has been found for the 2D case without gravity by Sen and Davis [39]. Experiments has been performed to validate the 3D case with gravity [40]. In this report a 2D simulation was performed without gravity. This simulation has been validated against the asymptotic solution and also compared against other numerical simulations.

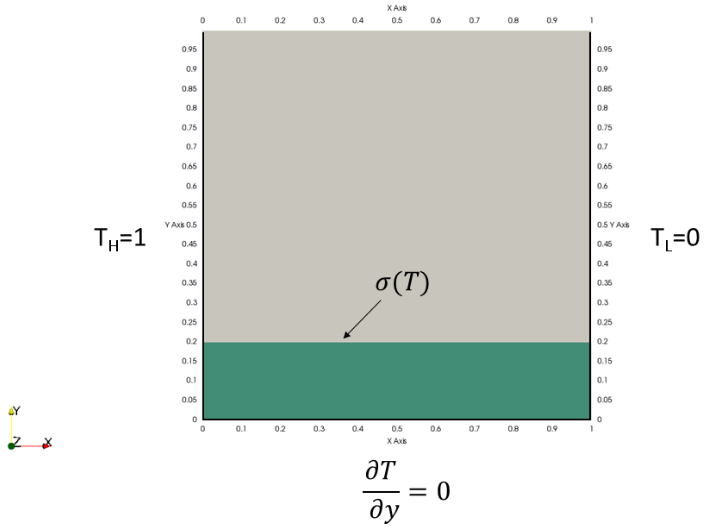

Figure 6.2: Thermo-capillary cavity flow setup with temperature boundary condition, grey indicate phase 1 and green phase 2.

In order to compare the results to the asymptotic solution and the literature numerical simulations with similar setup in terms of dimensionless quantities is required. The dimensionless numbers are:
The thermal-Reynolds number:

$$Re = \frac{\rho|\sigma|\Delta T h}{\mu^2} = 1, \tag{6.10}$$

Prandtl number:

$$Pr = \frac{\mu}{\rho a} = 0.2, \tag{6.11}$$

Marangoni number:

$$Ma = \frac{|\sigma|\Delta T h}{\mu a} = Re * Pr = 0.2, \tag{6.12}$$

and Capillary number:

$$Ca = \frac{|\sigma|\Delta T}{\sigma_{ref}} = 0.008. \tag{6.13}$$

Where $\Delta T = T_H - T_L$ and the aspect ratio is $A = h/L = 0.2$, where L is the length of the domain in the x direction. The dimensionless groups are used to determine the material parameters. The density and the viscosity of the fluid under the interface are set to unity. The material properties of the fluid above the interface are set to equal material properties of the fluid below the interface; however, the viscosity is set to zero. A linear varying temperature dependent surface tension is applied according to

$$\sigma(T) = \sigma_0 + \sigma_T(T - T_l), \tag{6.14}$$

where σ_0 and σ_T are set to satisfy the given dimensionless numbers.

6.2.1 Spatial and Temporal convergence

In order to verify that the mesh size and the simulation time step does not influence the solution, spatial and temporal convergence studies are performed. The temporal convergence test was performed by lowering the simulation time step ΔT until the position of the interface at steady state did not change. The temporal convergence study was performed on a uniform grid with grid size $\Delta = 5e^{-3}\,\mathrm{m}$. The time steps were $\Delta T = 50\,\mu\mathrm{s},\ 25\,\mu\mathrm{s},$ and $12.5\,\mu\mathrm{s}$.

The spatial convergence test was performed on a uniform grids. The grid size, Δx, was reduced until the position of the interface at steady state was not changed. The following grid sizes were considered $\Delta x = 0.02\,\mathrm{m},\ 0.01\,\mathrm{m},\ 5e^{-3}\,\mathrm{m},$ and $2.5e^{-3}\,\mathrm{m}$. The different mesh sizes can be seen in Figure 6.3.

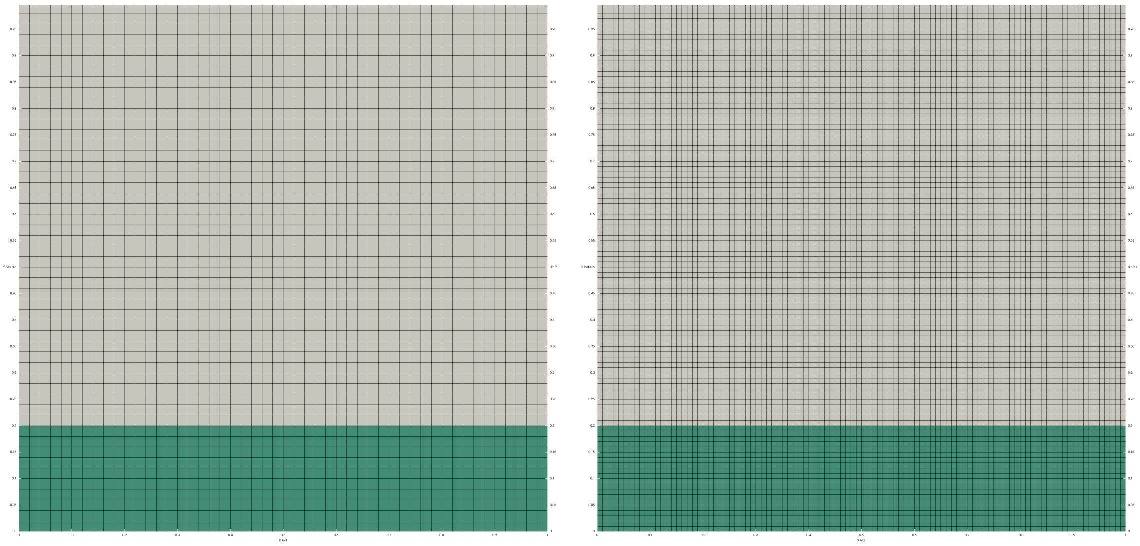

(a) 50x50

(b) 100x100

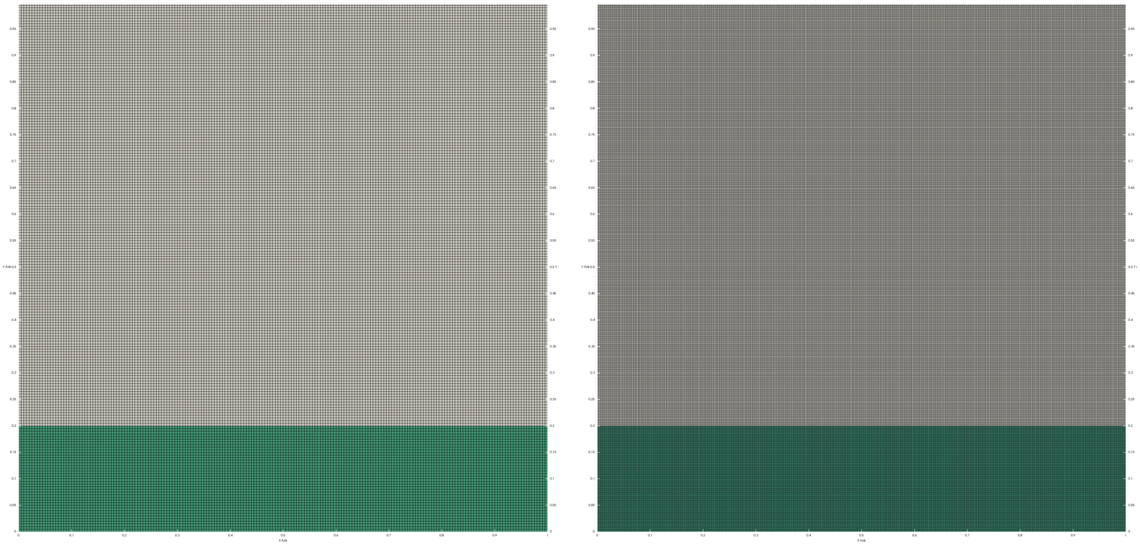

(c) 200x200

(d) 400x400

Figure 6.3: Mesh convergence study, mesh sizes.

6.3 Single line melt simulation

A single line melt simulation of the SLM process is performed with the improved normal surface tension force, temperature dependent surface tension, and the tangential component of the surface tension force. This simulation is performed to demonstrate metal AM melt pool modeling with low Bo number and high La number. In this section the setup of the single line melt simulation, the process parameters and the material properties of simulation are presented.

6.3.1 Simulation setup and process parameters

A single line melt simulation consists of a laser sweeping over a metal particle bed in a straight line. The particles melts as the laser heats them up and solidifies as the laser is removed and the heat is convected.

It is well know that a stochastic distribution of particles on the substrate will affect the characteristics of the melt such as width and depth of line melt. Despite this only a prearranged uniform particle placement pattern was used in the simulations. The particles in the simulation were closely packed so the packing density is close to experimental conditions where the particles will fill the bed. In an experimental setup the size of the metal particles varies, usually according to a normal distribution; however, in this simulation only mono-sized particles were considered. Only a single layer of particles was considered so that the particle diameter was the same as the layer height. The particle size was set to $D_p = 60\,\mu$m. The particle arrangement can be seen in Figure 6.4.

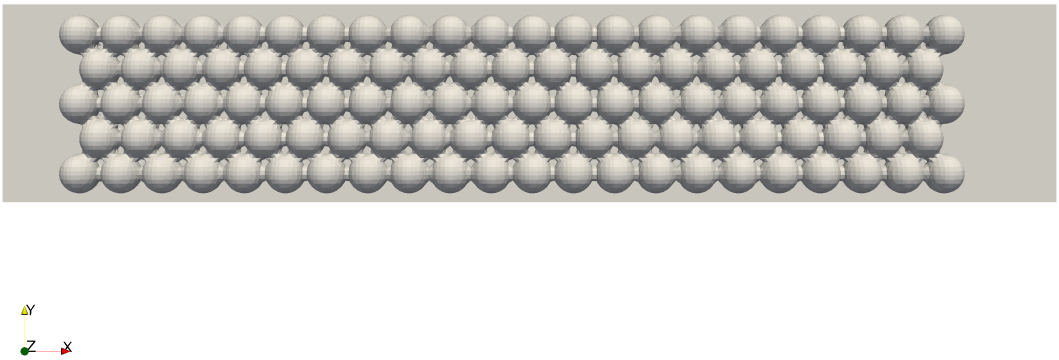

Figure 6.4: Particle bed bead arrangement

The laser was set to move with a speed of $V_L = 1m/s$. The laser spot diameter was set to $D_L = 150\,\mu$m and the laser power was set to $P_L = 225\,$W. The domain size was set to $N_x = 32$, $N_y = 6$, $N_z = 15$ with cell size $\Delta = 5e - 5$. The VOF edge was refined in three steps in order to more accurately capture the interface. The VOF edge refinement can be seen in Figure 6.5

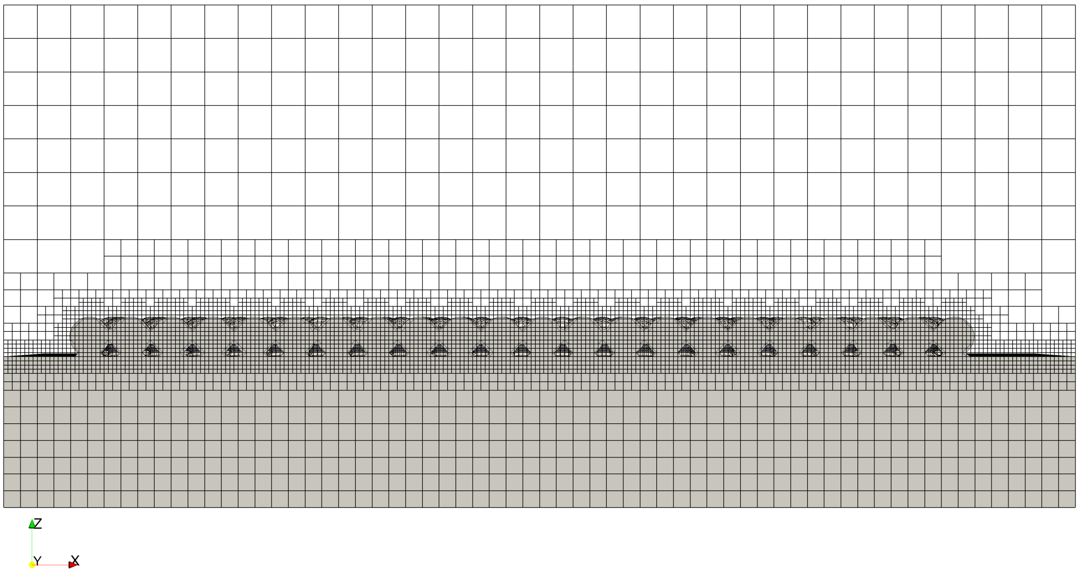

Figure 6.5: Mesh refinement at VOF edge

The initial simulation time step was set to $\Delta T = 0.1\,\text{ns}$. When the simulation started the time step was ramped up to $\Delta T = 7.5\,\text{ns}$ with a constant ramping step of 0.1 ns. This was done in order to simulate sharp temperature jump when the laser was turned on and also enable a faster simulation later.

Three simulation cases were performed: A gravity driven simulation were no surface tension forces are present, a constant surface tension simulation with only normal surface tension present, and a simulation with temperature dependent surface tension with both normal and tangential surface tension force. These simulation were performed in order to investigate the impact of different surface tension phenomena on the melt pool flow.

6.3.2 Material properties

The materials used for the SLM simulation were Ti-6Al-4V (Ti64) for the particles and the substrate, and Argon (Ar) for the surrounding gas in the building chamber. In order to properly model liquid Ti64 accurate thermo-physical material property values are required. The melting temperature of Ti64 is denoted T_m and has a value of $T_m = 1878\,\text{K}$. The temperature above which Ti64 is completely liquid i.e. the liquidus temperature denoted T_l is 1928 K. As the temperature of Ti64 increase the dynamic viscosity decreases. This relation is modeled with an Arrhenius model equation (4.19). The active energy for Ti64 is $\Delta E_a = 11153.7\,\text{J}$ and the nominal dynamic viscosity is to $\mu_0 = 1.665 \cdot 10^{-3}\,\text{PaS}$.

The surface tension of Ti64 decreases with increasing temperature. This relation is linear and is modeled using equation (5.16). For Ti64 the nominal surface tension is $\sigma_0 = 1.522\,\mathrm{Nm}$ and the surface tension variation with temperature is $\sigma_T = -5.5 * 10^{-4}\,\mathrm{Nm/K}$. The density of Ti64, denoted as ρ, is constant and has a value of $\rho = 4475\,\mathrm{kg/m^3}$. The thermal conductivity, denoted k, is also constant and attains a value of $k = 27\,\mathrm{W/mK}$. The specific heat capacity of the Ti64 is modeled according to equation (4.20) where the heat capacity $c_p = 730$ J/kgK latent heat, $L = 360000$ J/kg. In table 6.3 the material properties of Ti64 are summarized. The material properties of Ti64 are from references [41] and [23].

Table 6.3: Material properties of Ti-6Al-4V

Ti-6Al-4V			
Material property	Symbol	Value	Unit
Density	ρ	4475	kg/m^3
Viscosity (Nominal)	μ	1.665E-3	Pa s
Surface tension (Nominal)	σ	1.522	Nm
Thermal conductivity	k	27	W/mK
Heat capacity	c_p	730	J/kgK
Melting temperature	T_m	1878	K
Liquidus temperature	T_l	1928	K

In order to model the transport of the Ar and its temperature distribution the material properties of Ar is needed. All the material properties of the Ar are considered constant. The density of Ar attains a value of $\rho = 1.619\,\mathrm{kg/m^3}$. The dynamic viscosity of Ar is $\mu = 2.23 * 10^{-5}$ Pa s. The specific heat is $c_p = 523\,\mathrm{J/kgK}$ and the thermal conductivity is $k = 0.0172\,\mathrm{W/mK}$. Below in table 6.4 the material properties of Ar is summarized.

Table 6.4: Material properties of Argon

Argon			
Material property	Symbol	Value	Unit
Density	ρ	1.619	kg/m^3
Viscosity	μ	2.23E-5	Pa s
Thermal conductivity	k	0.0172	W/mK
Heat capacity	c_p	523	J/kgK

7

Results

In this chapter the results from the simulations described in chapter 6 are presented. The cases include curvature evaluation of a static drop in 2D and 3D, Thermocapillary cavity flow and SLM single line melt simulation.

7.1 Curvature Evaluation

The curvature at the VOF interface is numerically calculated for a static drop in equilibrium in both 2D and in 3D. The results from the different curvature calculation techniques mentioned in 6.1.1 and 6.1.2 are presented. First the 2D simulation results are presented, then follows the results from the 3D simulation.

7.1.1 Static Drop in 2D

In this section the results from the 2D simulation of the static droplet in equilibrium are presented. First the result from the mesh study is presented. Then the density ratio study results follows and lastly the results of the pressure evaluation is presented.

Mesh study

The L_1 and L_∞ norms of the curvature error for the five different mesh sizes are presented in Figure 7.1. In the Figure only the results from the simulations using the regular $\nabla\alpha$, $\nabla\tilde{\alpha}$ and the height function are presented.

As can be seen in Figure 7.1 when using height functions to calculate the curvature both the L_1 and the L_∞ error norms of the curvature error is lower compared to the respective error norms when calculating the curvature using the regular $\nabla\alpha$ and $\nabla\tilde{\alpha}$. When using height functions both the L_1 and the L_∞ error norms decreases as the grid resolution gets finer. The spatial convergence rate when using height functions is close to second order. When the curvature is calculated using $\nabla\alpha$ and $\nabla\tilde{\alpha}$ the L_1 and the L_∞ error norms increase when the gird resolution is finer.

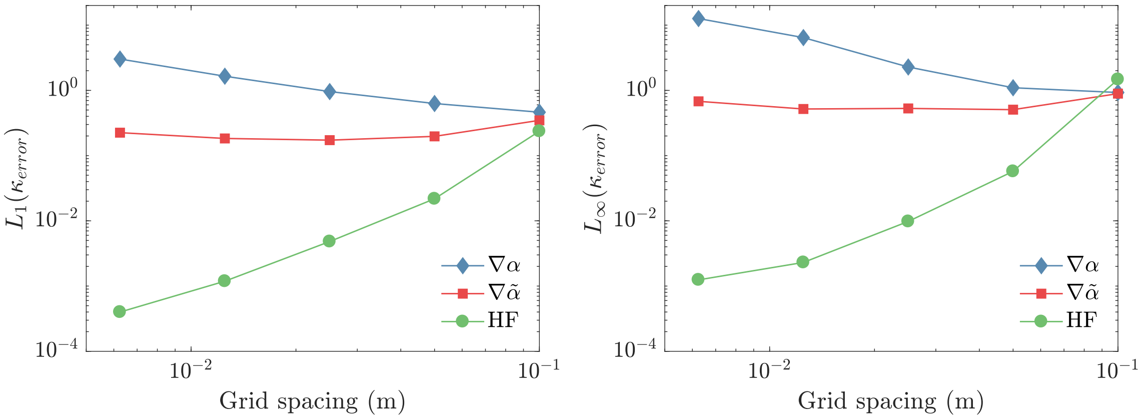

(a) L_1 error norm **(b)** L_∞ error norm.

Figure 7.1: Error norms of the curvature error κ_{error}, L_1, (left) and , L_∞, (right).

Density ratio study

In table 7.1 the L_1 and the L_∞ norms of the velocity for the different density ratios are presented.

Table 7.1: 2D: Error norms for different curvature calculation methods for increasing density ratios

Density ratio $\frac{\rho_2}{\rho_1}$	$L_1(\mathbf{u})$	$L_\infty(\mathbf{u})$
$\nabla\alpha$		
10^0	8.1272×10^{-3}	2.9244×10^{-2}
10^2	1.3180×10^{-1}	8.6831×10^{-1}
10^4	5.7831×10^{0}	5.0876×10^{1}
$\nabla\tilde{\alpha}$		
10^0	1.0043×10^{-3}	3.9598×10^{-3}
10^2	1.3184×10^{-2}	1.2476×10^{-1}
10^4	7.9473×10^{-1}	7.9891×10^{0}
HF		
10^0	9.9592×10^{-4}	2.6160×10^{-3}
10^2	2.4013×10^{-2}	1.2714×10^{-1}
10^4	1.6194×10^{0}	1.0068×10^{1}
HF - $\nabla\tilde{\alpha}$		
10^0	4.1629×10^{-4}	1.1045×10^{-3}
10^2	8.0545×10^{-3}	5.2262×10^{-2}
10^4	5.6824×10^{-1}	4.1225×10^{0}

As can be seen in table 7.1 both the L_1 and L_∞ error norms of the velocity increases as the density ratio increases for all the different curvature estimation methods. Both the L_1 and L_∞ error norms are lower when using height functions and further lowered with improved direction (HF - $\nabla\tilde{\alpha}$) as compared to when using the $\nabla\alpha$ and $\nabla\tilde{\alpha}$ curvature calculation techniques. It can be inferred from table 7.1 that the L_1

and L_∞ error norms are lowered more for lower density ratios for both the height functions techniques compared to using $\nabla\alpha$ and $\nabla\tilde{\alpha}$. For high density ratios the L_1 and L_∞ error norms are not reduced as much when using height functions. This means that as the density ratio is increased the height functions does not reduce the spurious current to the same degree as with low density ratios.

Pressure evaluation

In Figure 7.2 the pressure is plotted across the domain for the density ratio $\frac{\rho_2}{\rho_1} = 1$ at two different simulation times, $t = \Delta t$ and $t = 50\Delta t$. The sharp jump in pressure occurs due to the interface surface tension between the two phases.

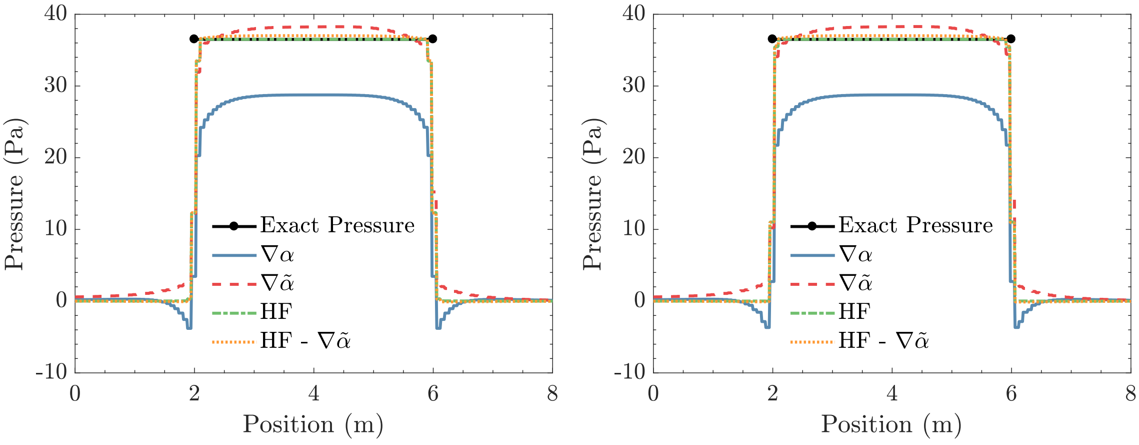

(a) Pressure across the domain at $t = \Delta t$.

(b) Pressure across the domain at $t = 50\Delta t$.

Figure 7.2: Pressure, numerical and exact across droplet $\frac{\rho_2}{\rho_1} = 1$

As can be seen in both Figure 7.2a (left) and 7.2b (right) when the density ratio $\frac{\rho_2}{\rho_1} = 1$ the pressure from $\nabla\tilde{\alpha}$ simulation is closer to the exact solution compared to $\nabla\alpha$ simulation for both simulation times. It can also be inferred that when using height functions the numerically calculated pressure is further closer to the exact pressure.

In Figure 7.3 the pressure is plotted across the domain for the density ratio $\frac{\rho_2}{\rho_1} = 10^2$ again at two different times, $t = \Delta t$ and $t = 50\Delta t$.

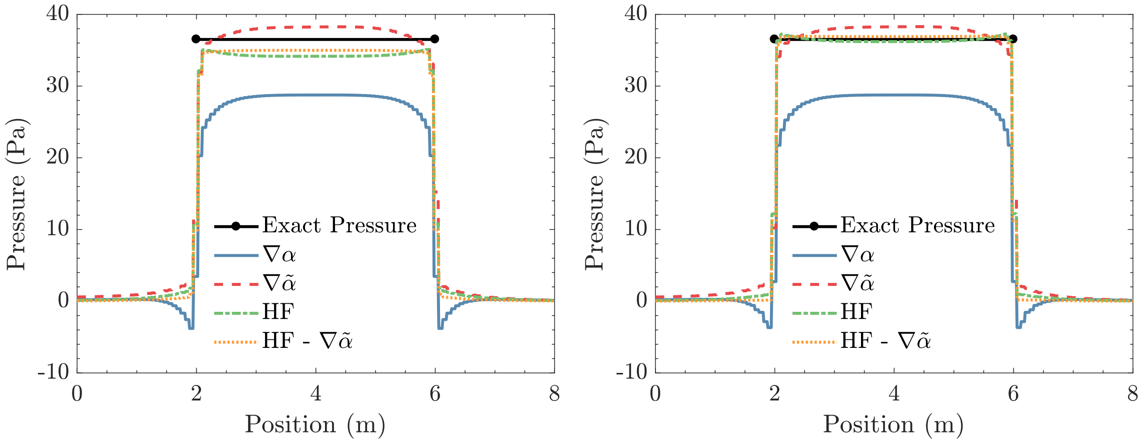

(a) Pressure across the domain at $t = \Delta t$.

(b) Pressure across the domain at $t = 50\Delta t$.

Figure 7.3: Pressure, numerical and exact across droplet $\frac{\rho_2}{\rho_1} = 10^2$

As can be seen in both Figure 7.3a (left) and 7.3b (right) when the density ratio $\frac{\rho_2}{\rho_1} = 10^2$, the $\nabla\tilde{\alpha}$ simulation is closer to the exact pressure compared to the $\nabla\alpha$ simulation at both $t = \Delta t$ and $t = 50\Delta t$. Using height functions results in an even more correctly predicted pressure. It can also be inferred that when the density ratio increases, from $\frac{\rho_2}{\rho_1} = 1$ to $\frac{\rho_2}{\rho_1} = 10^2$, the HF-$\nabla\tilde{\alpha}$ simulation performs better than HF especially at $t = \Delta t$. When comparing Figure 7.3a to 7.3b we see that the calculated pressure is closer to the exact pressure when $t = 50\Delta t$ than $t = 1\Delta t$ for all the curvature calculation methods. This is due to a numerical imbalance when initializing the volume fraction field on a discrete grid. The imbalance corrects itself as the simulation progresses.

In Figure 7.4 the pressure is plotted across the domain for the density ratio $\frac{\rho_2}{\rho_1} = 10^4$ again at two different simulation times, $t = \Delta t$ and $t = 50\Delta t$.

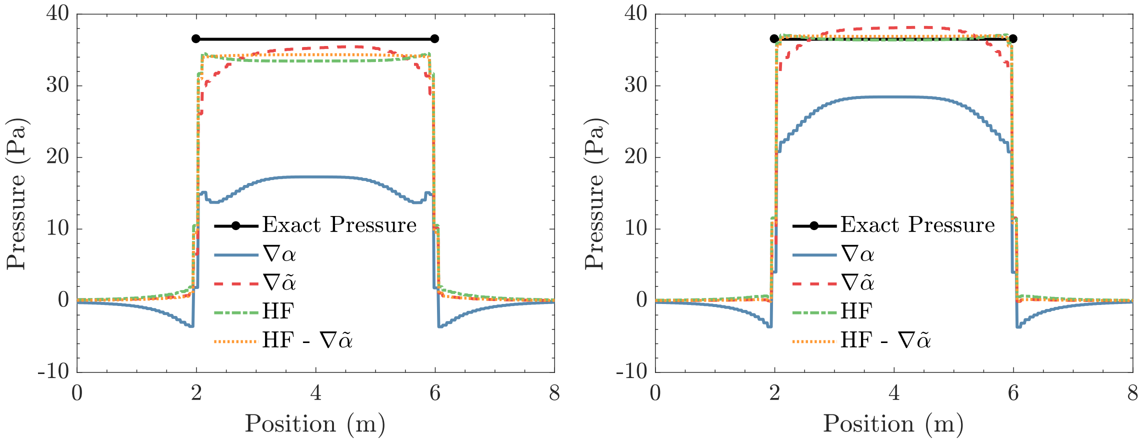

(a) Pressure across the domain at $t = \Delta t$.

(b) Pressure across the domain at $t = 50\Delta t$.

Figure 7.4: Pressure, numerical and exact across droplet $\frac{\rho_2}{\rho_1} = 10^4$

As can be seen in both Figure 7.4a (left) and 7.4b (right) when the density ratio $\frac{\rho_2}{\rho_1} = 10^4$, $\nabla\tilde{\alpha}$ is closer to the exact solution compared to $\nabla\alpha$ for both simulation times. Using height functions results in further better calculated pressure. When the density is further increased, from $\frac{\rho_2}{\rho_1} = 10^2$ to $\frac{\rho_2}{\rho_1} = 10^4$, the HF - $\nabla\tilde{\alpha}$ simulation result in better predicted pressure compared to HF. Again a numerical imbalance occurs due to the initialization of the volume fraction field at $t = \Delta t$. This imbalance is corrected when $t = 50\Delta t$.

From Figure 7.2-7.4 it can be inferred that the numerically calculated pressure deviates more from the exact pressure as the density ratio increases. It can be also be inferred that using height function improves the pressure calculation in terms of accuracy. The best performing curvature calculation technique to best approximate the pressure in 2D is the HF - $\nabla\tilde{\alpha}$ method as it on point with the regular HF method for low density ratios and slightly better in high density ratios.

7.1.2 Static Drop in 3D

In this section the results from the 3D simulation of the static droplet in equilibrium are presented. Firstly the results from the mesh study is presented. This is followed by the visualization of the curvature error and velocity vectors on the droplet. Then the result of the density ratio study is presented and lastly the pressure evaluation is presented.

Mesh Study

The L_1 and L_∞ norms of the curvature error for the five different mesh sizes are presented in Figure 7.5.

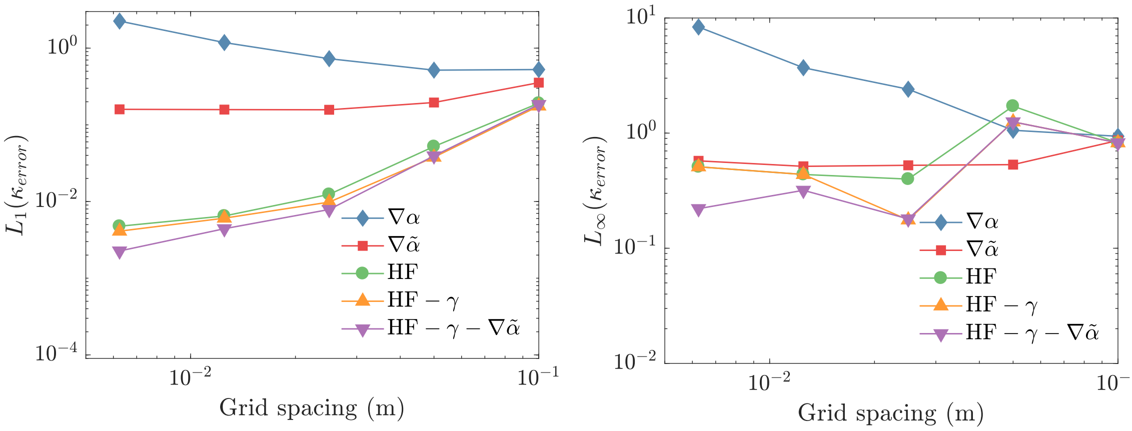

(a) L_1 norm of κ.

(b) L_∞ norm of κ.

Figure 7.5: L_1 norm of κ (left) and L_∞ norm of κ (right) for different curvature estimations calculations.

As can be seen in Figure 7.5 when using height functions to calculate the curvature the L_1 error norm of the curvature error is substantially lower compared to when calculating the curvature using the regular $\nabla\alpha$ and $\nabla\tilde{\alpha}$ for all the five different mesh sizes. When using height functions the L_1 error norm decreases as the grid resolution gets finer. The L_∞ error norm behaves more irregularly than the L_1 error norm. However, it can still be seen that the L_∞ error norm is reduced when using height functions. Overall the HF-$\gamma - \nabla\tilde{\alpha}$ has the lowest L_1 and L_∞ curvature error norms.

Visualization of curvature error and velocity vectors

In Figure 7.6 the curvature error is plotted on top of the 3D sphere for the $\nabla\alpha$, HF, HF-γ, and HF-$\gamma - \nabla\tilde{\alpha}$ curvature calculation techniques.

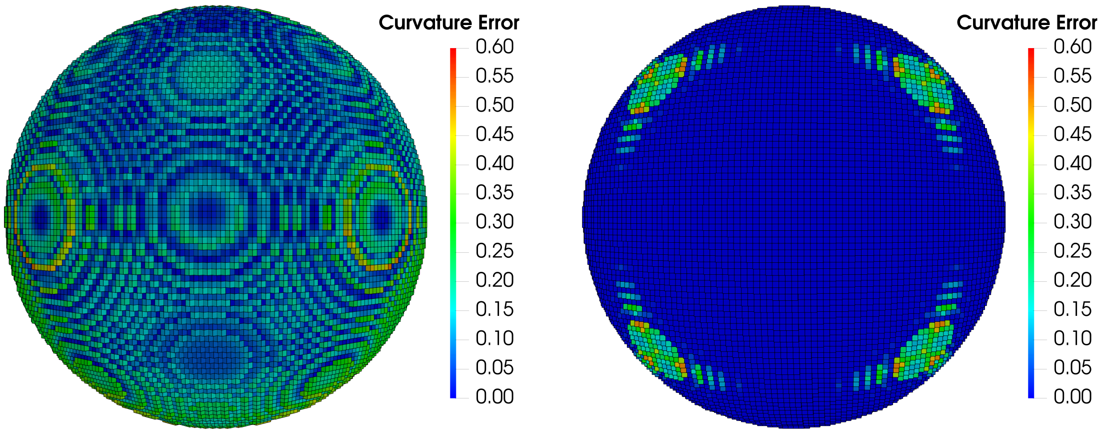

(a) $\nabla\alpha$

(b) HF.

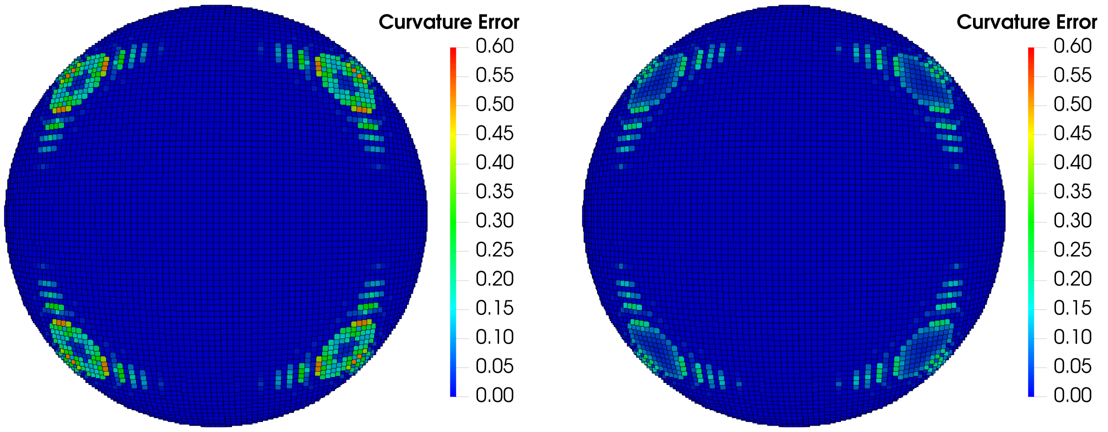

(c) HF - γ.

(d) HF - γ - $\nabla\tilde{\alpha}$.

Figure 7.6: Curvature error, κ_{error}, using different curvature calculation techniques

In Figure 7.6 we see where the curvature error is reduced when using height functions. The areas where the curvature error remains large can also be seen and how these areas are further improved when using HF$-\gamma - \nabla\tilde{\alpha}$.

In Figure 7.7-7.9 the velocity vector at the VOF interface is plotted for a 2D cut section of the sphere. Three different curvature calculation methods are compared, the $\nabla\alpha$, $\nabla\tilde{\alpha}$, and HF$-\gamma-\nabla\tilde{\alpha}$ methods. Further more the velocity vector are plotted for three different density ratios $\frac{\rho_2}{\rho_1} = 1$, $\frac{\rho_2}{\rho_1} = 10^2$, and $\frac{\rho_2}{\rho_1} = 10^4$.

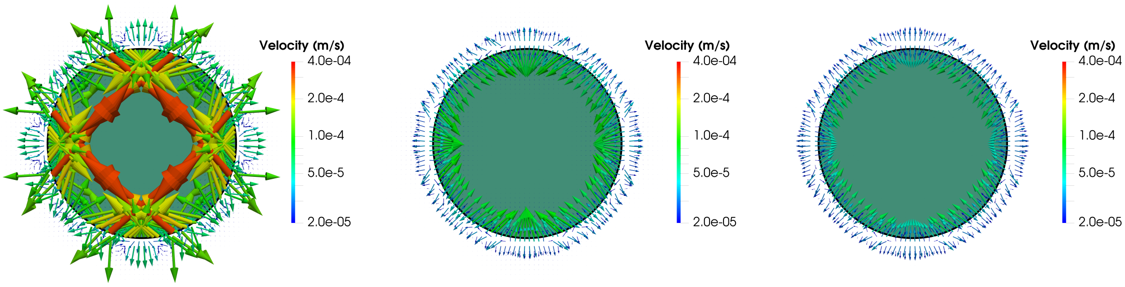

(a) $\nabla\alpha$. **(b)** $\nabla\tilde{\alpha}$. **(c)** HF - γ - $\nabla\tilde{\alpha}$.

Figure 7.7: Velocity around VOF edge, curvature calculated using, $\nabla\alpha$, (left), $\nabla\tilde{\alpha}$ (middle), and using Height functions for $\rho_2/\rho_1 = 1$.

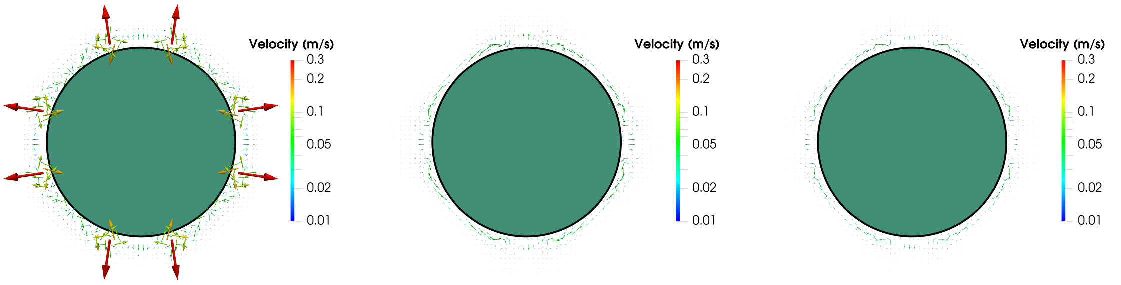

(a) $\nabla\alpha$. **(b)** $\nabla\tilde{\alpha}$. **(c)** HF - γ - $\nabla\tilde{\alpha}$.

Figure 7.8: Velocity around VOF edge, curvature calculated using, $\nabla\alpha$, (left), $\nabla\tilde{\alpha}$ (middle), and using Height functions for $\rho_2/\rho_1 = 10^2$.

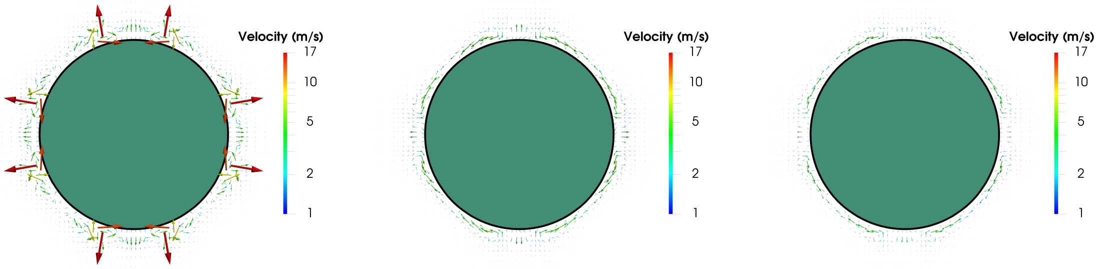

(a) $\nabla\alpha$. **(b)** $\nabla\tilde{\alpha}$. **(c)** HF - γ - $\nabla\tilde{\alpha}$.

Figure 7.9: Velocity around VOF edge, curvature calculated using, $\nabla\alpha$, (left), $\nabla\tilde{\alpha}$ (middle), and using Height functions for $\rho_2/\rho_1 = 10^4$.

From Figure 7.7-7.9 it can be inferred that the spurious currents around the VOF edge increase as the density ratio increases. Furthermore it shows that using $\nabla\tilde{\alpha}$ to calculate the curvature reduces the spurious currents and using HF-$\gamma - \nabla\tilde{\alpha}$ further reduces the spurious currents around the VOF edge.

Density ratio study

In table 7.2 the L_1 and the L_∞ norms of the velocity for the density ratios $\frac{\rho_2}{\rho_1} = 1$, $\frac{\rho_2}{\rho_1} = 10^2$, and $\frac{\rho_2}{\rho_1} = 10^4$ are presented.

Table 7.2: 3D: Error norms for different curvature calculation methods for increasing density ratios

Density ratio $\frac{\rho_2}{\rho_1}$	$L_1(\mathbf{u})$	$L_\infty(\mathbf{u})$
$\nabla\alpha$		
10^0	3.4408×10^{-3}	1.1465×10^{-2}
10^2	4.5483×10^{-2}	4.4301×10^{-1}
10^4	2.0243×10^{0}	3.4093×10^{1}
$\nabla\tilde{\alpha}$		
10^0	6.3156×10^{-4}	1.6895×10^{-3}
10^2	1.3161×10^{-2}	6.4854×10^{-2}
10^4	9.3642×10^{-1}	6.0108×10^{0}
HF		
10^0	1.3126×10^{-3}	2.9471×10^{-3}
10^2	3.2100×10^{-2}	1.5581×10^{-1}
10^4	2.2417×10^{0}	1.3531×10^{1}
HF - γ		
10^0	1.3091×10^{-3}	2.9473×10^{-3}
10^2	3.2111×10^{-2}	1.5582×10^{-1}
10^4	2.2438×10^{0}	1.3531×10^{1}
HF - γ - $\nabla\tilde{\alpha}$		
10^0	5.0812×10^{-4}	1.3316×10^{-3}
10^2	1.0587×10^{-2}	5.6445×10^{-2}
10^4	7.8292×10^{-1}	5.2524×10^{0}

As can be seen in table 7.2 both the L_1 and L_∞ error norms of the velocity increases as the density ratio increase for all the different curvature estimation methods. Both the L_1 and L_∞ error norms are lower when using height functions and further lowered with HF - $\nabla\tilde{\alpha}$ and HF - $\gamma - \nabla\tilde{\alpha}$ as compared to when using the $\nabla\alpha$ curvature calculation techniques.

Pressure ratio evaluation

In Figure 7.10 the pressure is plotted across the domain for the density ratio $\frac{\rho_2}{\rho_1} = 1$ at two different times, $t = \Delta t$ and $t = 50\Delta t$.

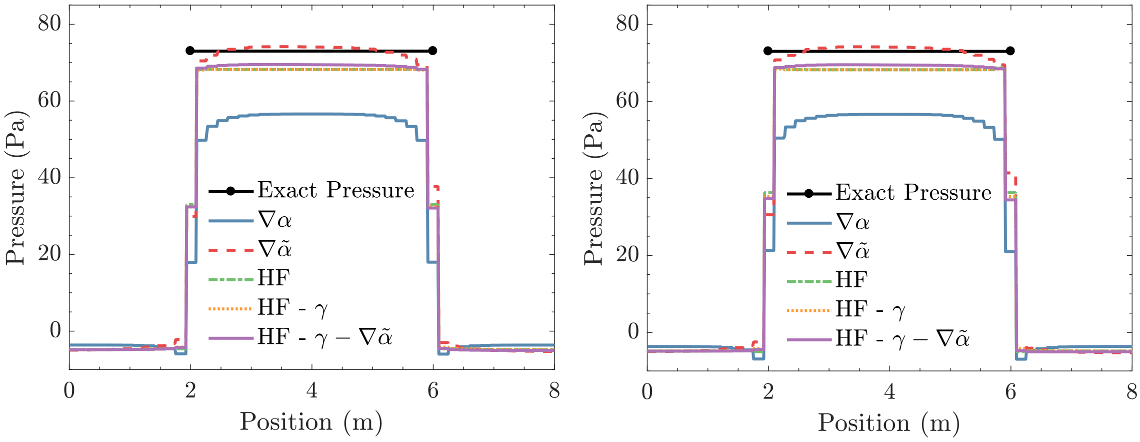

(a) Pressure across the domain at $t = \Delta t$.

(b) Pressure across the domain at $t = 50\Delta t$.

Figure 7.10: Pressure, numerical calculations and exact across drop $\frac{\rho_2}{\rho_1} = 10^0$

As can be seen in both Figure 7.10a (left) and 7.10b (right) when the density ratio $\frac{\rho_2}{\rho_1} = 1$ the pressure from $\nabla\tilde{\alpha}$ simulation is closest to the exact pressure. However, the $\nabla\tilde{\alpha}$ simulation fails to produce a sharp pressure jump. When using height functions the numerically calculated pressure jump is sharp and closer to the exact pressure than the $\nabla\alpha$ simulation.

In Figure 7.11 the pressure is plotted across the domain for the density ratio $\frac{\rho_2}{\rho_1} = 10^2$ again at two different times, $t = \Delta t$ and $t = 50\Delta t$.

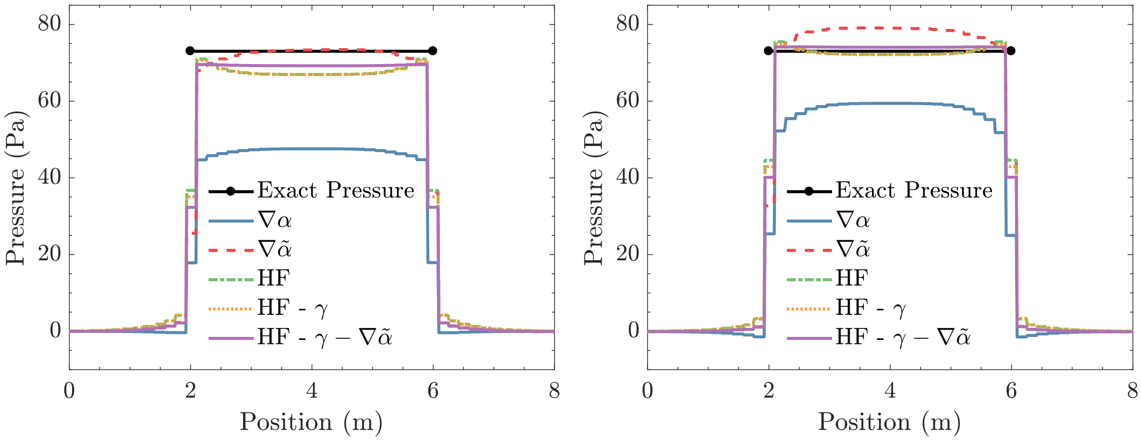

(a) Pressure across the domain at $t = \Delta t$.

(b) Pressure across the domain at $t = 50\Delta t$.

Figure 7.11: Pressure, numerical calculations and exact across drop $\frac{\rho_2}{\rho_1} = 10^2$

As can be seen in both Figure 7.11a (left) and 7.11b (right) when the density ratio $\frac{\rho_2}{\rho_1} = 10^2$, the height function simulations produce a sharp pressure jump for both simulation times. At $t = 50\Delta t$ the height functions pressure calculation are close to the exact pressure. As the density ratio increases, from $\frac{\rho_2}{\rho_1} = 1$ to $\frac{\rho_2}{\rho_1} = 10^2$, the height function simulation performs better. As in 2D the pressure correct itself at $t = 50\Delta t$ compared to $t = \Delta t$ due to the initialization of a volume fraction field on a discrete grid.

In Figure 7.12 the pressure is plotted across the domain for the density ratio $\frac{\rho_2}{\rho_1} = 10^4$ again at two different simulation times, $t = \Delta t$ and $t = 50\Delta t$.

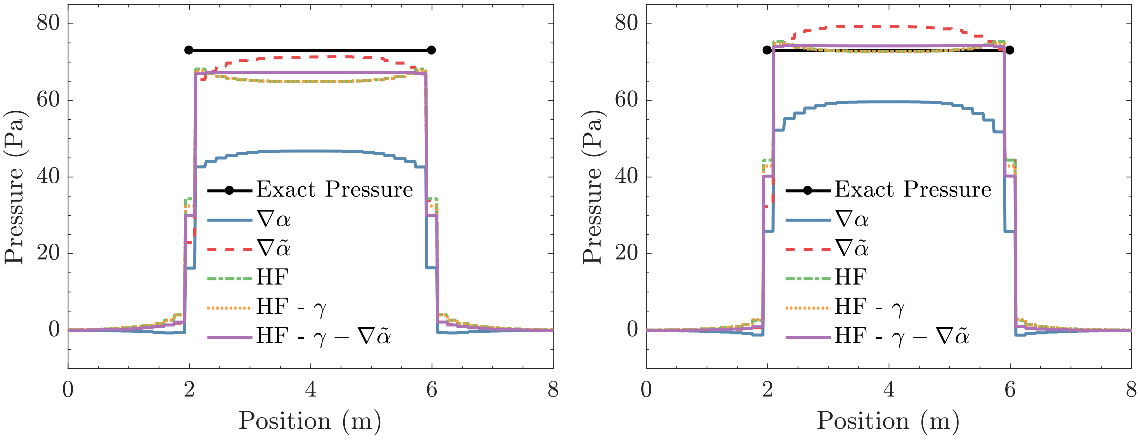

(a) Pressure across the domain at $t = \Delta t$.

(b) Pressure across the domain at $t = 50\Delta t$.

Figure 7.12: Pressure, numerical calculations and exact across drop $\frac{\rho_2}{\rho_1} = 10^4$

As can be seen in both Figure 7.12a (left) and 7.12b (right) when the density ratio $\frac{\rho_2}{\rho_1} = 10^4$, the height function simulations produce a sharp pressure jump and again the calculated pressure is close exact pressure at $t = 50\Delta t$. Again the pressure correct itself after $t = 50\Delta t$ due to the initialization of a volume fraction field on a discrete grid.

From Figure 7.10-7.12 it can be inferred that when using height functions to calculate the curvature a sharp pressure jump is achieved. At $t = 50\Delta t$ the height functions simulations produce a pressure close to the exact pressure when the density is $\frac{\rho_2}{\rho_1} = 10^2$ and $\frac{\rho_2}{\rho_1} = 10^4$. The overall best curvature calculation technique to best approximate the pressure is the HF - $\gamma - \nabla\tilde{\alpha}$ method as it produces a sharp pressure jump and of the height function techniques is closest to the exact pressure.

7.2 Thermo-capillary cavity flow

Thermo-capillary cavity flow simulations with three different time steps were performed. The height of the interface along x at steady state for the three different time steps are shown in Figure 7.13. The boxes in Figure 7.13a are enlarged in Figure 7.13b and 7.13c.

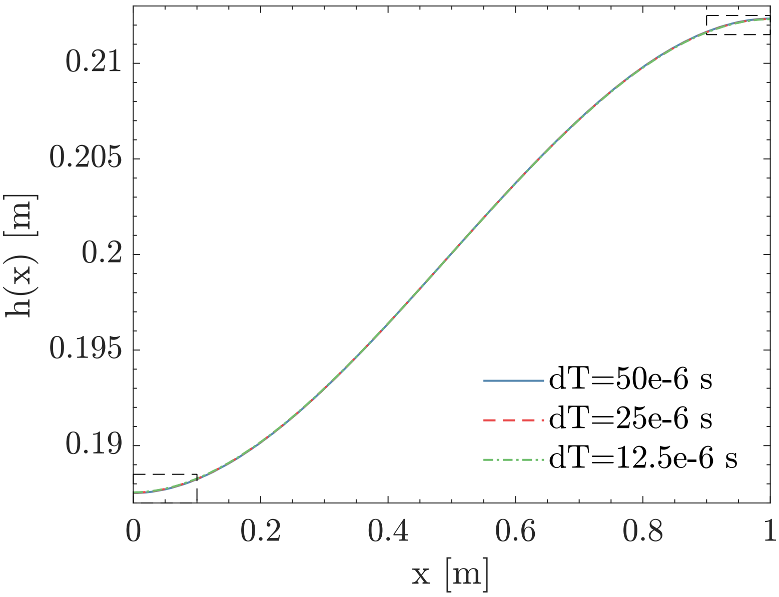

(a) Temporal convergence study, height of interface along x

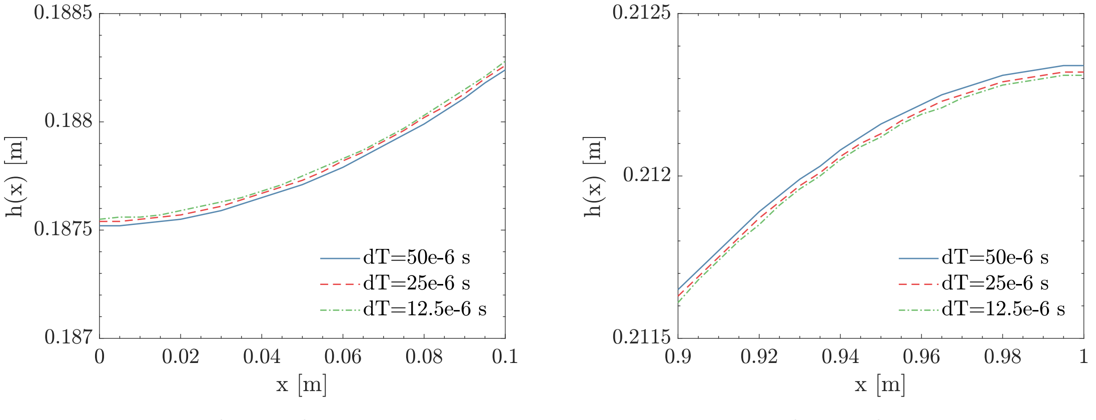

(b) Height of interface near $x = 0$.

(c) Height of interface near $x = L$.

Figure 7.13: Temporal convergence study

In Figure 7.13 we see that the difference between the interface height using three different time step is small. Thus has the solution converge in terms of time step size.

A mesh study of the thermo-capillary cavity flow was conducted. The thermo-capillary cavity flow simulation was performed with four different grid sizes. The height of the interface along x at steady state for the four different mesh sizes is shown in Figure 7.14. The boxes in Figure 7.14a are enlarged in Figure 7.14b and 7.14c.

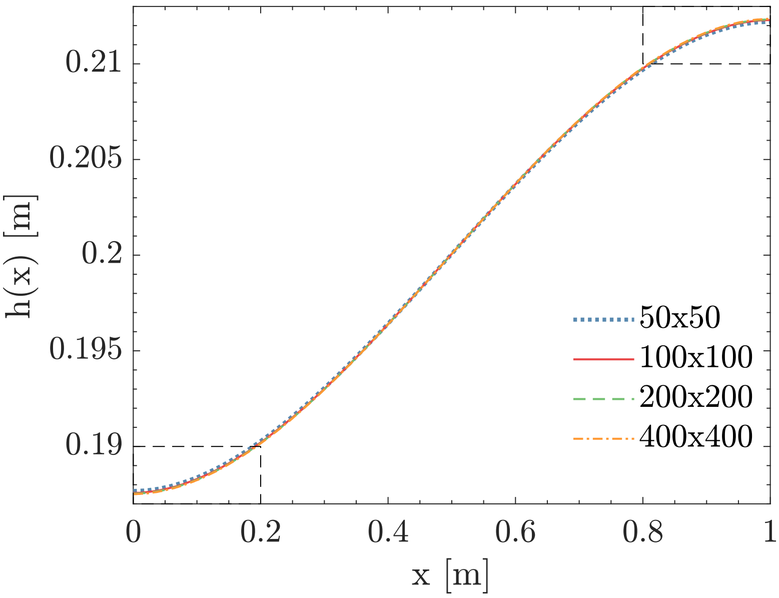

(a) Height of interface along x

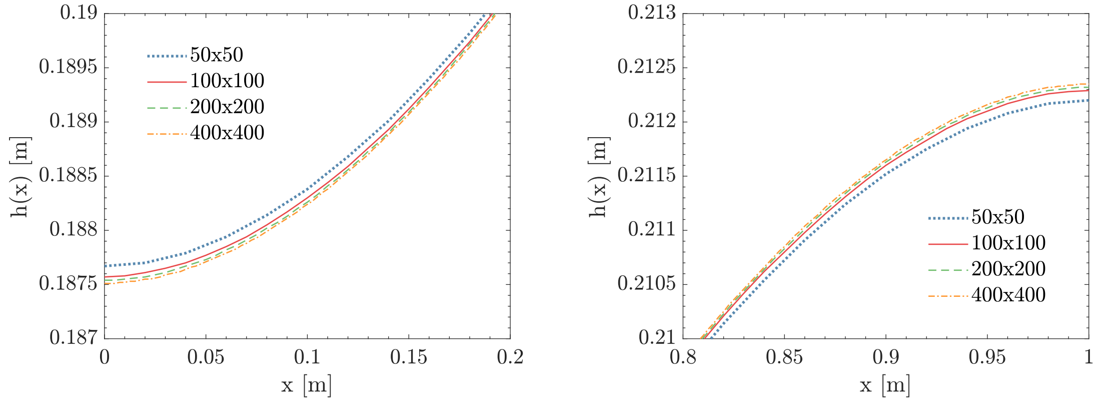

(b) Height of interface near $x = 0$. **(c)** Height of interface near $x = L$.

Figure 7.14: Mesh convergence study

From Figure 7.14 we see that the difference in interface height for the different grid sizes is small. In table 7.3 the height of the interface at the two end points $x = 0$ and $x = L$, for the four different grid sizes are presented.

Table 7.3: Mesh study thermo-capillary cavity

Mesh Study		
Mesh Size\Height	h(x=0)	h(x=L)
50x50	0.18767	0.21220
100x100	0.18757	0.21229
200x200	0.18754	0.21232
400x400	0.18751	0.21235

The difference in height is small enough indicating that the solution has converged with respect to mesh size. Thus has a solution which is independent of the mesh size and time step been obtained. The height at the end points of the cavity is compared against literature in table 7.4. As can be seen in 7.4 the solution from IBOFlow is almost identical to the analytic solution by Sen and Davis [39].

Table 7.4: Height at cavity ends comparison

Height at cavity ends comparison		
Analytical solution	h(x=0)	h(x=L)
Sen and Davis (Eq. 5.3c) [39]	0.188	0.213
Numerical solutions	h(x=0)	h(x=L)
IBOFlow	0.188	0.212
Sasmal and Hochstein [37]	0.174	0.224
Truchas [38]	0.187	0.209

7.3 Single line melt

In this section the result of the single line melt simulations are presented. The curvature in the single line melt simulation was calculated using the HF$-\gamma - \nabla\tilde{\alpha}$ method. Three different simulations were performed, a gravity driven simulation with no surface tension active, a constant surface tension simulation, and a temperature dependent surface tension simulation with thermo-capillary force. The result of the gravity driven simulation at three different time steps can be seen in Figure 7.15.

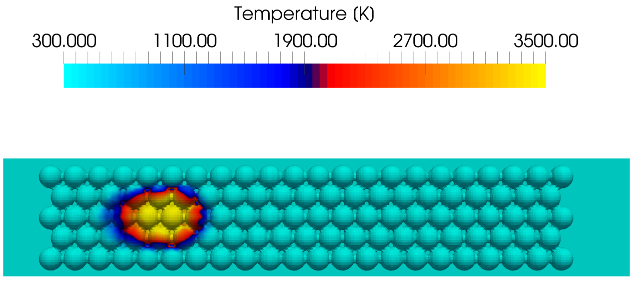

(a) Simulation time: $t = 20000\Delta t$

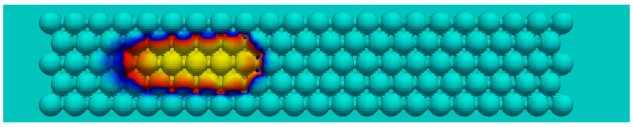

(b) Simulation time: $t = 40000\Delta t$

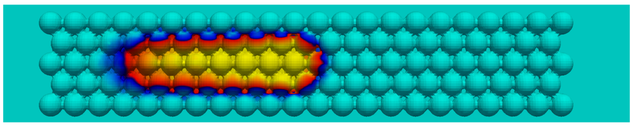

(c) Simulation time: $t = 60000\Delta t$.

Figure 7.15: Single line melt with no surface tension

In Figure 7.15 the liquid metal flow is calm, and does only flow downwards. This is because the only present force on the liquid metal is gravity. No other outer forces are acting on the flow. The gravity force is weak since the metal particles are small and will thus not cause strong forces on the flow. In Figure 7.16 the result of constant surface tension simulation is presented for three different time steps.

In Figure 7.16 the liquid metal flow is more chaotic. As the laser traverses across the substrate the metal particles are heated above their melting temperature and

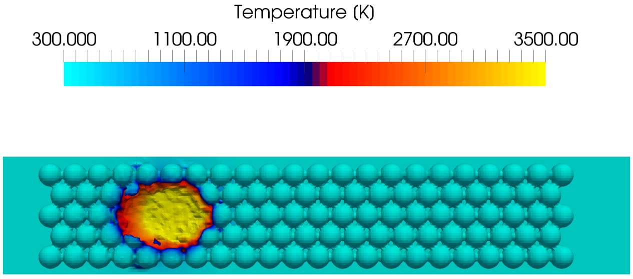

(a) Simulation time: $t = 20000\Delta t$

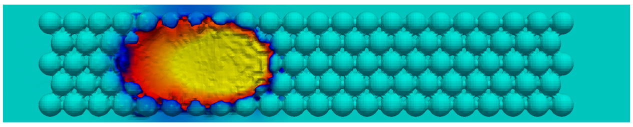

(b) Simulation time: $t = 40000\Delta t$

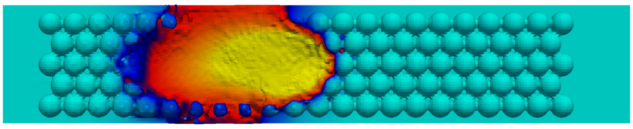

(c) Simulation time: $t = 60000\Delta t$.

Figure 7.16: Single line melt with constant surface tension

start to melt. The liquid metal is pulled by the surface tension force, which greatly affect the flow. However, as the surface tension is constant only a normal surface tension force is present and no tangential movement of the surface can occur. In Figure 7.17 the result of the temperature dependent surface tension single line melt simulation is presented.

In Figure 7.17 the liquid metal flow is again chaotic. Temperature dependent surface tension cause tangential movement of the liquid metal flow. The liquid metal is warmest at the center of the laser spot causing the surface tension to be lowest there. With the tangential surface tension force present the surface is pulled towards the location with the highest surface tension, i.e outwards from the current laser spot position. This causes a deeper penetration into the metal particles and the substrate as liquid is pulled away from the laser spot. This in turn causes keyholing phenomena. Keyholing occurs when a heat source penetrates deep into a substrate causing a deep hole. The hole is then partially covered by flowing liquid collapsing if the hole gets too deep. The liquid metal then rapidly solidifies when the heat source is removed. This causes empty pockets and porosity which in turn cause poor mechanical performance of the finished part.

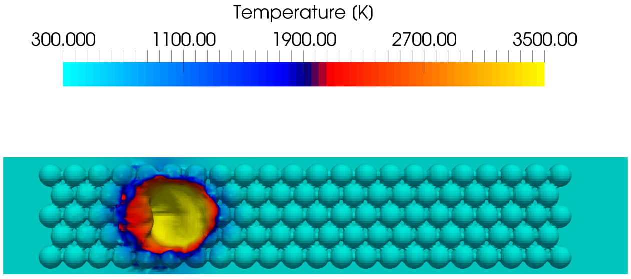
Temperature (K)
300.000
1100.00
1900.00
2700.00
3500.00

(a) Simulation time: $t = 20000\Delta t$

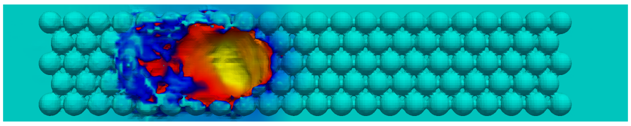

(b) Simulation time: $t = 40000\Delta t$.

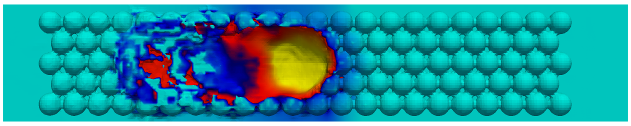

(c) Simulation time: $t = 60000\Delta t$.

Figure 7.17: Single line melt with temperature dependent surface tension

From Figure 7.15-7.17 it is inferred that the surface tension has a strong impact on the metal flow during metal AM. A temperature dependent surface tension results in a further detailed description of how the liquid behaves.

8

Conclusion

The surface tension framework in IBOFlow is extended and improved. An improved method for calculating the curvature is assessed and evaluated. The new curvature calculation method is compared to analytical results of a static drop in equilibrium. Grid studies of the new curvature calculation method show that the curvature error is further reduced as the grid gets finer in both 2D and 3D. Studies on the density ratio between the phases show that the spurious currents are reduced. However, as the density ratio between the phases increase the improvement is less pronounced and the magnitude of the spurious currents is still fairly large. Further more the pressure is evaluated across the droplet and compared to analytical exact result. With the new curvature calculations the numerically calculated pressure is closer to the exact value in both 2D and 3D.

A temperature dependent surface tension model together with a thermo-capillary surface tension force is proposed and validated. The temperature dependent surface tension model together with the thermo-capillary surface tension are validated using a thermo-capillary cavity flow benchmark case. Spatial and temporal convergence test show excellent convergence. The results are compared to analytical solution and show almost perfect agreement. Thus are the temperature dependent surface tension model and the thermo-capillary surface tension force correctly modeled.

The new surface tension framework is used to simulate a single line melt of a selective laser melting process. First is a simulation without any surface tension performed. Only gravity drives the melt flow in this simulation. Then a constant surface tension simulation is performed. Lastly a temperature dependent surface tension simulation is performed. The results of the three simulations were compared and the effect of the surface tension on the melt pool flow is evaluated. With the extended surface tension framework the melt pool flow is more dynamic concluding that temperature dependent surface tension and thermo-capillary surface tension force are important when modeling metal AM.

Even though melt pool simulations were demonstrated, with a full surface tension force model, further addition of physical model are required to accurately simulate the melt flow behaviour. A proposed next step is to implement a vapour pressure model into the framework to account for the evaporation of the liquid metal.

The density study with the new curvature method indicate that the although the curvature has been improved something else is causing artificial velocities to appear.

A possible suggestion is that the discretization technique currently used is causing the velocities to appear. This needs to be further investigated.

Bibliography

[1] Gu D. D., Meiners W., Wissenbach K. and Poprawe R. (2012) "Laser additive manufacturing of metallic components: material, processes and mechanisms", International Material Reviews, vol. 57, no. 3, pp. 133-164

[2] Herzog D., et al, (2016), "Additive manufacturing of metals", Acta Materialia 117, pp. 371-392

[3] Thompson S., Bian L., Shamsaei N., Yadollahi A., (2015), "An overview of Direct Laser Deposition for additive manufacturing; Part 1: Transport phenomena, modeling and diagnostics", Additive Manufacturing 8, pp. 36-62

[4] Qui C., Panwisawas C., Ward M., Ward H., Basoalto H., Brooks J., and Attallah M., (2015), "On the role of melt flow into the surface structure and porosity development during selective laser melting", Acta Materialia 96, pp. 72-79

[5] Körner C., and Heinl E. A. P., (2011), "Mesoscopic simulation of selective beam melting process", Journal of Materials Processing Technology 211, pp. 978-987

[6] Körner C., et al, (2013), "Fundamental consolidation mechanisms during selective beam melting of powders", Modelling Simul. Mastr. Sci. Eng. vol. 21

[7] Zeng K., Pal D., and Stucker B., (2012), "A review of thermal analysis methods in Laser Sintering and Selective Laser Melting", National science foundation solid freeform fabrication symposium, Austin, TX, 6–8 August. Austin, TX: Laboratory for Freeform Fabrication.

[8] Tang M., Pistorius C., Beuth J., (2016), "Prediction of lack-of-fusion porosity for powder bed fusion", Additive Manufacturing 14, pp. 39-48

[9] Schoinochoritis B., Chantiz D., and Salonitis K., (2014), "Simulation of Metallic Powder Bed Additive Manufacturing Processes with the Finite Element Method: a critical review", Institution of Mechanical Engineers, pp. 1-22

[10] Khairallah S., and Anderson A., (2014), "Mesocopic simulation model of selective laser melting of stainless steel powder", Journal of Material Processing Technology 214, pp. 2627-2636

[11] Khairallah S., Anderson A., Rubenchik A., and King W., (2016), "Laser powder-bed fusion additive manufacturing: Physics of complex melt flow and formation mechanisms of pores, spatter, and denudation zones", Acta Materialia 108

[12] Mark, A., and van Wachem B.G.M., (2008), "Derivation and validation of a novel implicit second-order accurate immersed boundary method", Journal of Computational Physics, vol. 227, no. 13, pp. 6660-6680.

[13] Mark A., Rundqvist R., Edelvik F., (2011), "Comparison between different immersed boundary conditions for simulation of complex fluid flows", Journal of Fluid Dynamics & Materials Processing, vol. 7, no. 3, pp. 241-258.

[14] Svenning E., Mark A., Edelvik F., Glatt E., Rief S., Wiegmann A., Martinsson L., Lai R., Fredlund M., Nyman U., (2012), "Multiphase simulation of fiber suspension flows using immersed boundary methods", Nordic Pulp and Paper Research Journal, vol. 27, no. 2, pp. 184-191.

[15] Johnson T., Röyttä P., Mark A., Edelvik F. (2016), "Simulation of the Spherical Orientation Probability Distribution of Paper Fibers in an Entire Suspension Using Immersed Boundary Methods", Journal of Non-Newtonian Fluid Mechanics, no. 1.

[16] Mark A., Andersson B., Tafuri S., Engström K., Söröd H., Edelvik F., Carlson J.S. (2013), "Simulation of Electrostatic Rotary Bell Spray Painting in Automotive Paint Shops", Atomization and Sprays, vol. 23, no. 1, pp 25-45.

[17] Mark A., Bohlin R., Segerdahl D., Edelvik F., Carlson J.S., (2014), "Optimisation of robotised sealing stations in paint shops by process simulation and automatic path planning", International Journal of Manufacturing Research, vol. 9, no. 1, pp. 4-26.

[18] Göhl J., Mark A., Sasic S., Edelvik F., (2018), "An immersed boundary based dynamic contact angle framework for handling complex surfaces of mixed wettabilities", International Journal of Multiphase Flow, vol. 109, pp. 164-177.

[19] Körner C. (2016), "Additive manufacturing of metallic components by selective electron beam melting - a reivew", International Materials Review, vol. 61, no. 5, pp. 361-377

[20] Berman B. et al,(2012), "3D printing: the new industrial revolution", Bus. Horizons 55, pp. 155-162

[21] Ibarra-Medina J., (2013), "Development and application of CFD model of laser metal deposition", PhD Thesis, Manchester, UK: The University of Manchester

[22] Frazier W.,(2014), "Metal Additive Manufacturing: A Review", Journal of Materials Engineering and Performance, Vol. 23, no. 6, pp. 1917-1928

[23] Wunderlich R., (2008) "Surface Tension and Visosity of Industrial Ti-Alloys Measured by the Oscillating Drop Method on Board Parabolic Flights", High Temperature Material and Processes Special Issue vol. 27, no. 6

[24] Markl M., and Körner C., (2016) "Multi-Scale Modeling of Powder-Bed-Based Additive Manufacturing", Annual Review of Materials Research

[25] Davidson L., (2018) "Fluid mechanics, turbulent flow and turbulence modeling", Downloaded from: `http://www.tfd.chalmers.se/~lada/MoF/text_book.html`

[26] Hirt C.W., and Nichols B.D., (1981), "Volume of fluid (VOF) method for the dynamics of free boundaries", Journal of Computational Physics, vol. 39, no. 1, pp. 201-225.

[27] Rhie C.M., and Chow, W.L., (1983), "Numerical study of the turbulent flow past an airfoil with trailing edge separation", AIAA Journal, vol. 21, no. 11, pp.1525-1532.

[28] Ubbink O., and Issa R.I., (1999), "A Method for Capturing Sharp Fluid Interfaces on Arbitrary Meshes", Journal of Computational Physics, vol. 153, no. 1, pp. 26-50.

[29] Brackbill J.U., Kothe D.B., and Zemach, C., (1992), "A continuum method for modeling surface tension", Journal of Computational Physics, vol. 100, no. 2, pp. 335-354.

[30] Bidare P., Bitharas I., Ward R.M., Attallah M.M,Moore A.J., (2018), "Fluid and particle dynamics in laser powder bed fusion", Acta Materialia, pp. 107-120

[31] Afkhami S., and Bussmann M., (2008), "Height functions for applying contact angles to 3D VOF simulations", Int. J. Numer. Meth. Fluid

[32] López J., et al, (2009), " An improved height function technique for computing interface curvature from volume fractions", Comput. Methods Appl. Mech. Engrg. vol. 198, pp. 2555-2564

[33] López J., Hernández J., (2010), "On reducing interface curvature computation errors in height function technique", Journal of Computational Physics 229, pp. 4855-4868

[34] Keene B. J.l, (1993), "Review of data for the surface tension of pure metals", International Materials Reviews, vol. 38, no. 4, pp. 157-192,

[35] Francois M., Cummins S., Dendy E., Kothe D., Sicilian J., Williams M., (2005), "A balanced-force algorithm for continuous and sharp interfacial surface tension models within a volume tracking framework", Journal of Computational Physics 213, pp. 141-173

[36] Mundrane M., and Zebib A., (1997), "Two- and three-dimensional buoyant thermocapillary convection", Physics of Fluids 9, pp. 1277

[37] Sasmal G.P., and Hochstein J.I., "Marangoni convection with a curved and deforming free surface in a cavity, Journal of Fluids Engineering, vol. 116, pp. 5

[38] Marianne F., James S., Douglas K., (2006), "Modeling of thermocapillary forces within a volume tracking algorithm", TMS (The minerals, metals and material society)

[39] Asok S., and Stephen D., (1981), " Steady thermocapillary flows in two-dimensional slots", J. Fluid Mech., vol. 121, pp. 163-186

[40] Gillon P., and Homsy G.M., (1997), "Combined thermocapillary-buoyancy convection in a cavity: An experimental study", Physics of Fluids 9, pp. 1277

[41] Boivineau M., et. al., (2006), "Thermophysical Properties of Solid and Liquid Ti-6Al-4V (TA6V) Alloy", International Journal of Thermophysics, vol. 27, no. 2,